nature biomedical engineering

Article

https://doi.org/10.1038/s41551-026-01612-y

X-ray activated platinum complex induces DNA damage and enhances cancer immunotherapy through abscopal effect

Received: 2 January 2024

Accepted: 7 January 2026

Guiyuan Chen[1], Xiangxia Li[1], Yu Huang[2], Cheng Zheng[3], Haopeng Fang[4], Qiaoyun Zhang[4], Ke Liu[5], Kecheng Wu[1], Qilong Zhu[1], Changqing Guo[1], Huanjun Zhu[1], Ruike Dai[1], Ying He[1], Qiuhong Zhu[6], Wenchao Zhou[6], Yidong Yang[3], Zibo Li[7], Kun Qu[5] ✉, Bofeng Li[4] ✉, Shiyan Xiao[2] ✉, Shaomin Tian[8], Bengang Xing[9,10], Xiaoyuan Chen[11,12,13,14], Andrew Z. Wang[15], Yujie Xiong[16] & Yuanzeng Min[1] ✉

Radiotherapy is used in more than half of cancer patients, yet most radiosensitizers increase reactive oxygen species (ROS) to enhance cytotoxicity in treated cells. This approach has limited use in hypoxic tumours and may cause oxidative injury to healthy tissues. We developed a platinum(II) azido complex (Complex 1) that releases platinonitrene upon X-ray exposure. Platinonitrene reacts with nucleophilic sites on DNA bases, forming covalent adducts that disrupt DNA integrity and cause double-strand breaks, leading to tumour cell death through a mechanism distinct from classical platinum coordination. Computational modelling elucidated this pathway and supported its role in radiosensitization. Complex 1 was synthesized by sequential ligand exchange of potassium tetrachloroplatinate with cyclohexanediamine, silver nitrate and sodium azide. In murine models, complex 1 showed negligible toxicity to major organs and normal immune cells while selectively reducing regulatory T-cell infiltration in tumours. Combined with low-dose radiotherapy and programmed cell death protein 1 blockade, it achieved complete regression of bilateral tumours in 40% of mice, demonstrating a strong abscopal effect. This work establishes metallonitrene-based, ROS-independent radiosensitization for precision radiotherapy.

Radiotherapy (RT), which uses high-energy radiation or radioactive energy to induce tumour cell death via DNA damge[1,2], plays a decisive role in cancer treatment, but it rarely induces complete tumour regression on metastatic tumour[3–5]. Emerging reports demonstrated that immune checkpoint inhibitors (ICIs) can synergize with RT and boost the abscopal effect, a rare phenomenon where RT to primary tumour inhibits the growth of distant metastatic tumours, to generate complete tumour regression[6–9]. However, clinical application of RT is still hampered by optimization of the delivery dose to decrease radiation toxicity to realize more personalized and precise RT[10]. The difficulty in determining radiosensitivity in different types of tumour is an important biological challenge[11]. Therefore, the development of a radiosensitizer[12,13] that could sensitize low-dose RT within the local area, is a major need.

Metallonitrene with a subvalent atomic nitrogen ligand, which is generated upon irradiation (for example, ultraviolet radiation (UVR)[14]),

A full list of affiliations appears at the end of the paper. ✉e-mail: qukun@ustc.edu.cn; libf@ustc.edu.cn; xiaosy@ustc.edu.cn; minyz@ustc.edu.cn

is a critical catalytic intermediate in chemical synthesis and participates in many important reactions as singlet or triplet intermediates[14–21]. The enhanced electrophilicity of active atomic nitrogen makes metallonitrenes powerful reactive intermediates for various N-atom transfer reactions such as N-N coupling reactions[22–24]. Therefore, metallonitrenes have high potential to react with bases of DNA in vivo to form stable chemical bonds and lead to twisted fractures of DNA, thus possessing potential to enhance DNA damage and thereby sensitize RT. The intrinsic reactivity of metallonitrenes might offer some opportunities for metallodrug discovery for sensitization of RT[25,26]. However, current research with metallonitrenes mainly focus on UVR activation, which is impossible for in vivo application.

Here, as a proof of concept, we designed a Pt(ii)-N$_3$ complex *cis*-[(1R,2R)-1,2-cyclohexanediamine-N,N′][N$_3$]$_2$ platinum (**1**) that can produce platinonitrene from radiolysis only upon receiving RT, which facilitated its application in vivo (Fig. 1a)[27,28]. A density functional theory (DFT) simulated the generation of platinonitrene, which is bonded to DNA by N-N coupling (Pt-N-N-DNA), distinct from the classic Pt-N coordination structure where Pt binds to nucleophilic sites on DNA via coordination interaction to induce DNA platination. This process enhanced DNA damage to sensitize RT in vivo for primary tumour therapy, which is independent of reactive oxygen species[29] (ROS) and can produce more immunogenic cell death (ICD) to release danger signals, for example, high mobility group box-1 protein (HMGB1) and calreticulin (CRT). The sensitization promoted more immune cell infiltration and elicited stronger immune responses[2,30]. Note that the radiolysis intermediate platinonitrene could only be produced in areas subjected to RT. The complex **1** itself does not show obvious antitumour efficacy without RT, but effectively inhibited infiltration of regulatory T cells, which benefitted the inhibition of metastatic tumour growth, thereby enhancing the abscopal effect with up to 40% complete regression with long-lasting immune memory effects in vivo.

Results

Complex 1 can generate platinonitrene post RT and induce DNA platination

To verify the generationof platinonitrene upon RT, **1** was mixed with dimethyl sulfide (DMS) in water at pH 5.5. The product of platinonitrene and DMS was detected by mass spectrometry (MS), which indicated that **1** could produce platinonitrene upon RT (Fig. 1b). The ultraviolet spectrum of **1** also changed upon RT (Supplementary Fig. 1). The N-N coupling products of platinonitrene and bases (cytosine) were analysed by high-performance liquid chromatography (HPLC) and confirmed by MS (Fig. 1c and Supplementary Figs.2–6). The natural bond orbital analysis of complex **2** based on DFT calculations showed a single covalent Pt-N σ bond, and an s-type lone pair and two singly occupied *p*-type natural localized molecular orbitals (NLMOs) on the N atom, as well as four essentially non-bonding Pt *d* orbitals (Extended Data Fig. 1a–e). These results demonstrated the platinonitrene character of Pt(II)-N for **2**, with a Pt-N Mayer bond order of 1.15 (Fig. 1d). Similarly, natural bond orbital analysis supported the notion of a [Pt(II)-N] platinonitrene for complex **3** (Extended Data Fig. 1f,g). To target **1** towards the DNA duplex, we performed molecular dynamic (MD) 'flooding' simulations[31] of a 48mer oligoDNA with a large number of **1** in solution, and identified that **1** is coordinated with amine groups of cytosine bases at the major groove of the GC step (Fig. 1e,f).

Two distinct pathways via N-N coupling are proposed for the reactions between platinonitrene and cytosine bases (Fig. 1g,h). The N-N coupling product **I2** is formed with a barrier of 9.4 kcal mol^{-1} in a highly exergonic step (ΔG = 69.5 kcal mol^{-1}, Fig. 1g). This nitrene-mediated intermolecular N-N coupling has also been suggested in hydrazide synthesis[22] and aldehyde amidation[14] using platinonitrene. Fig 1h displays an alternative pathway of Pt(II)-N attacking the amine group of another coordinated cytosine base, in which the intermolecular N-N coupling step is mediated by a radical hydrogen atom abstraction (HAA) from the amine group to metallonitrene. For metallonitrene **3**, the first direct N-N coupling reaction with a free-energy barrier of 12.3 kcal mol^{-1} leads to the intermediate **I4** (Fig. 1i). Attack of the other Pt(II)-N towards cytosine is achieved through the HAA reaction with a slight free-energy barrier of 2.6 kcal mol^{-1}, followed by a downhill N-N coupling, leading to the final product **I5′** (Fig. 1i). Either the single or the double intermolecular N-N coupling reaction between the metallonitrene and cytosine amine groups produces covalent bonding between them, thereby interrupting the physiological activities of DNA in cellular systems.

Sensitization of 1 to RT induces enhanced ICD and DNA damage

We investigated the apoptosis that was induced by sensitization of **1** to RT. Flow cytometry analysis showed that **1** itself induced negligible apoptosis. Apoptosis induced by **1** + RT was greatly enhanced, and the proportions of late apoptosis cells reached 2.4-fold that of the RT-alone group (Fig. 2a). Co-administration of **1** with RT notably induced the inversion of mitochondrial membrane potential (Fig. 2b,c), resulting in changes in mitochondrial membrane permeability, which further indicated that co-administration of **1** with RT could promote mitochondrial damage and effectively induce apoptosis in tumour cells. We also found that **1** could effectively deplete superoxide anions (O_2^-) and ROS in tumour cells after RT (Fig. 2d,e and Supplementary Figs.7–9), which suggests that **1**-sensitized RT is not ROS dependent.

Fluorescence analysis of tumour tissues with confocal laser scanning microscopy (CLSM) showed a considerable increase in the expression of CRT and HMGB1 (Fig. 2f and Supplementary Fig.10). Immunofluorescence of Ki67 and Caspase-3 was also analysed (Fig.2g). ELISA suggested that **1**-sensitized RT effectively promoted the release

Fig. 1 | Generation of platinonitrene with complex 1 upon RT and its DNA platination via N-N coupling. a, Scheme of **1** reacted with DNA upon RT. **b**, The trapping of platinonitrene produced upon RT based on DMS was verified by mass spectrometry. **c**, The mass spectrometry data of products of **1** reacting with cytosine upon RT. Complex **1** could react with cytosine after RT to form two types of products, Pt-N-N-C and Pt-N-N-CC, rather than the classic Pt-N coordination structure. **d**, Computed spin density distribution (isosurface at 0.01 a_0^{-3}) and NPA spin population, at the level of PBE0-D/def2-TVZPP. Atom colour code: green, Pt; tan, C; blue, N; white, H. **e**, Structural representative snapshot of the binding mode between **1** and DNA duplex in licorice, derived from classical MD simulations. The typical coordination of **1** with base pairs is shown in the dashed box. The platinum atoms are represented as a bead in cyan whereas the nitrogen atoms of azide and primary amine groups are in blue. The carbon, oxygen and hydrogen atoms are colored in tan, red and white, respectively. The distances of azide groups in **1** from DNA are r1 and r2, respectively. **f**, Distribution of the locations of **1** when interacting with DNA duplex. 'WG' and 'MG' refer to the major and minor grooves of the 'd(GC)' segment, respectively. **g**–**i**, Calculated reaction mechanism of platinonitrene compound **2** (**g** and **h**, at singlet and triplet states) and **3** (**i**, at singlet and quintet states) with cytosine bases. 'TS' and 'I' stand for transition state and intermediate, respectively. Note that the DNA backbone is not shown, and the nitrene N atom of the platinonitrene compound **2** orients towards the upper cytosine base in **g** and the bottom cytosine base in **h**. For platinonitrene **2**, N-N coupling can occur at the upper (**g**) or the lower (**h**, first proton transfer from amine to nitrene via HAA, followed by downhill N-N coupling) cytosine of the GC step. The singlet N-N coupling products (**I2** and **I3′**) are thermodynamically favoured over their triplet states (**g**,**h**). For platinonitrene **3**, the proton transfer from the amine group of the upper cytosine towards nitrene assists the N-N bonding between them (**I4**). **I4** first experiences the HAA process (**I4**→**I5**), and then intramolecular N-N coupling to achieve the final product **I5′**. For metallonitrene **3**, the singlet pathway is kinetically and thermodynamically favoured over the quintet pathway (singlet surface in red, triplet surface in black, and quintet surface in orange; ΔG in kcal mol^{-1}).

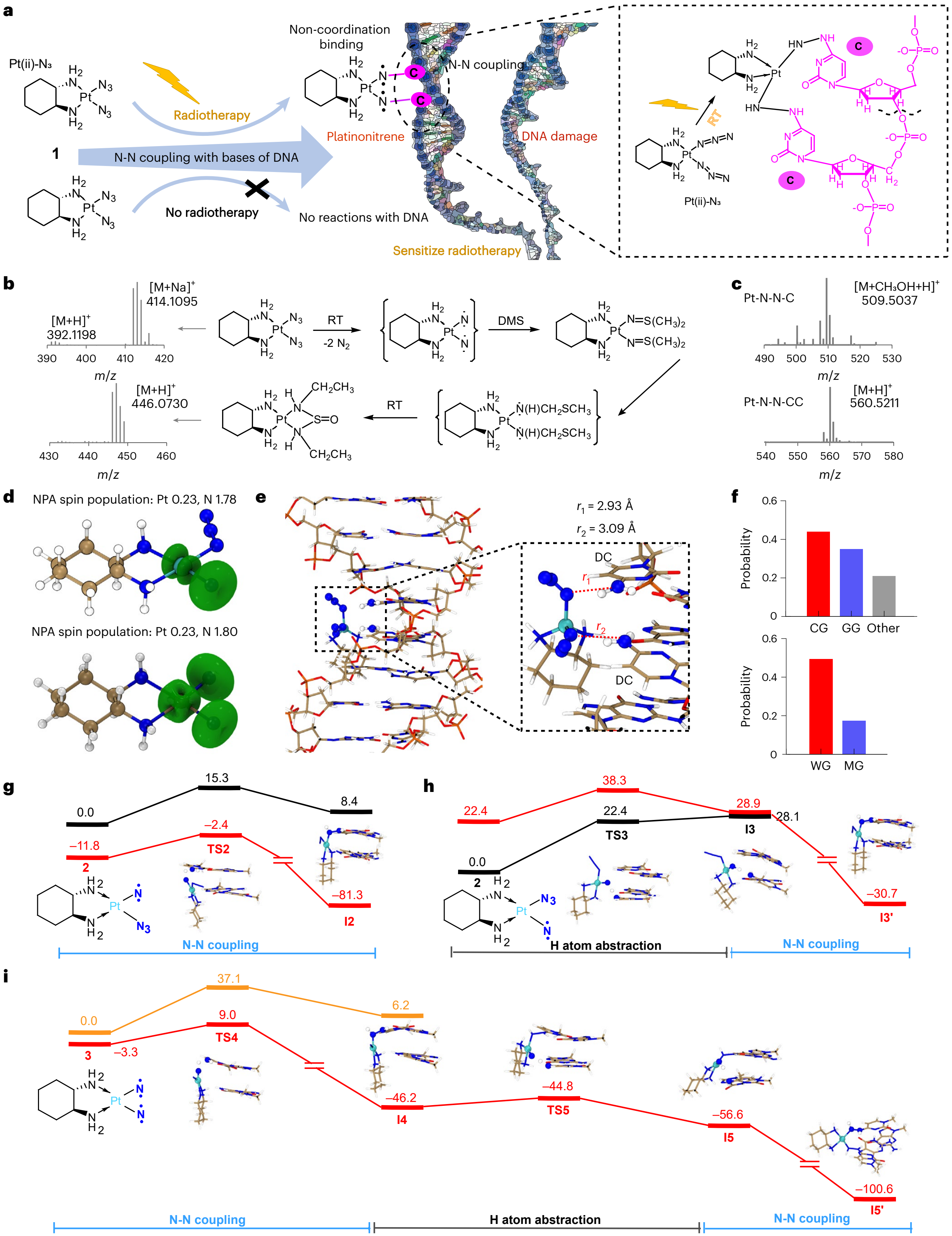
a
Pt(II)-N₃
1
Radiotherapy
N-N coupling with bases of DNA
No radiotherapy
Non-coordination binding
N-N coupling
Platinonitrene
DNA damage
No reactions with DNA
Sensitize radiotherapy
RT
Pt(II)-N₃
b
[M+Na]⁺ 414.1095
[M+H]⁺ 392.1198
390 400 410 420
m/z
RT
-2 N₂
DMS
N=S(CH₃)₂
[M+H]⁺ 446.0730
430 440 450 460
m/z
CH₂CH₃
S=O
RT
N(H)CH₂SCH₃
c
Pt-N-N-C
[M+CH₃OH+H]⁺ 509.5037
490 500 510 520 530
m/z
Pt-N-N-CC
[M+H]⁺ 560.5211
540 550 560 570 580
m/z
d
NPA spin population: Pt 0.23, N 1.78
NPA spin population: Pt 0.23, N 1.80
e
r₁ = 2.93 Å
r₂ = 3.09 Å
DC
DC
f
Probability
0 0.2 0.4 0.6
CG GG Other
WG MG
g
0.0
15.3
8.4
–11.8
–2.4
–81.3
2
TS2
I2
N-N coupling
h
22.4
38.3
28.9
28.1
0.0
22.4
2
TS3
I3
–30.7
I3'
H atom abstraction
N-N coupling
i
0.0
37.1
6.2
9.0
–3.3
3
TS4
–46.2
I4
–44.8
TS5
–56.6
I5
–100.6
I5'
N-N coupling
H atom abstraction
N-N coupling

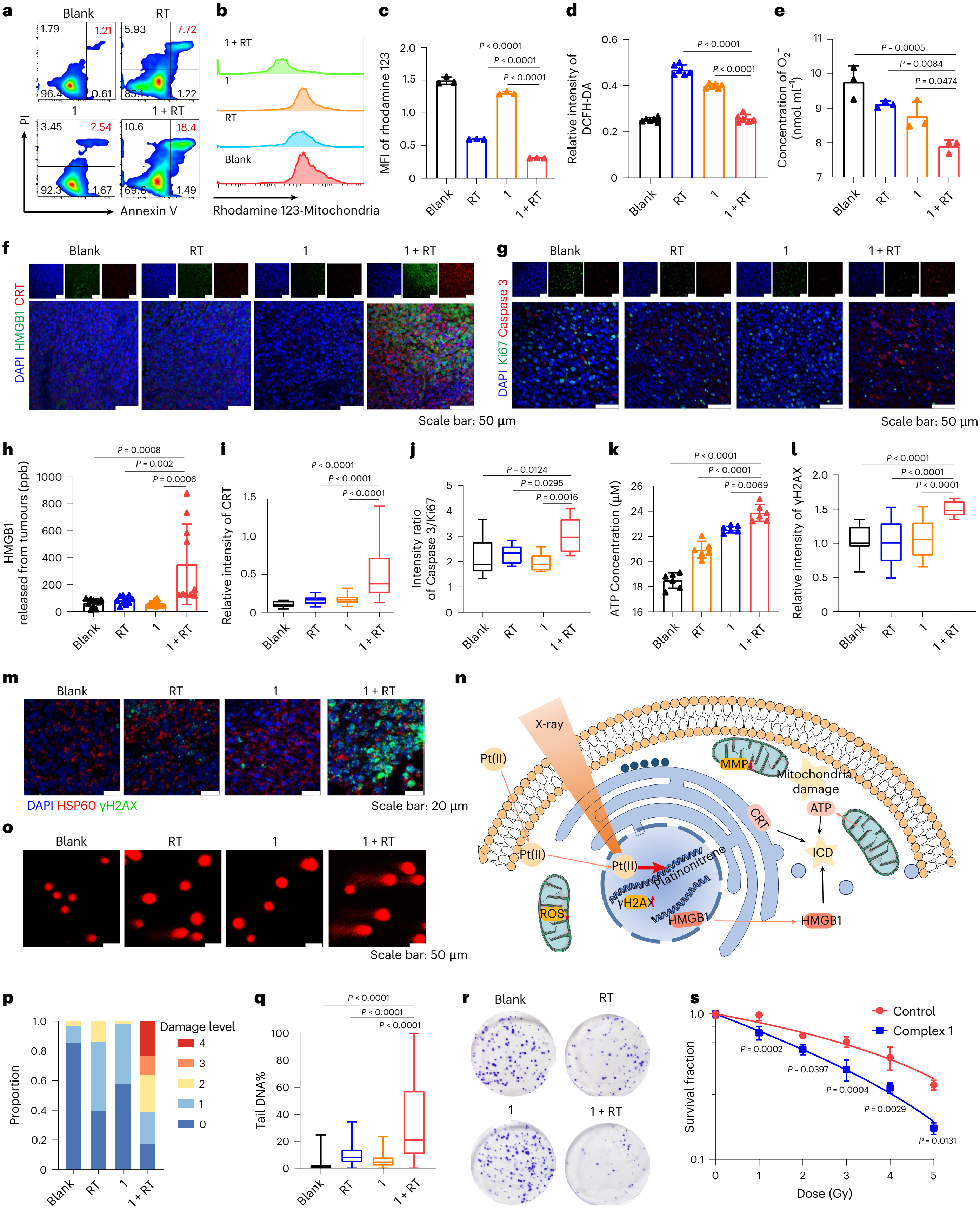

of HMGB1 in tumour tissues (Fig. 2h) and quantitative analysis of fluorescence intensity showed a 2–3-fold increase in the expression of CRT (Fig. 2i), which suggested that **1** could effectively sensitize RT with enhanced apoptosis and cytotoxicity. The average fluorescence intensity ratio of caspase-3 to Ki67 demonstrated that tumours treated with **1** + RT showed lower expression of Ki67 and higher expression of caspase-3, which indicated that the tumour cells had a higher apoptotic ratio and a weaker tendency to proliferate. However, the

Fig. 2 | Complex 1-sensitized RT induces enhanced cytotoxicity, exhibits stronger DNA damage and induces more robust immunogenic cell death in CT26 cells. a, Annexin V FITC/PI staining analysis of apoptosis. **b**, Representative flow histogram showing reduced mitochondrial membrane potential after **1**-sensitized RT in CT26 cells. **c**, Corresponding mean fluorescence intensity (MFI) of **b** (*n* = 3). **d**,**e**, Concentrations of ROS (**d**, *n* = 6) and O_2^- (**e**, *n* = 3) in CT26 cells, indicating ROS/O_2^- consumption by **1**-sensitized RT. **f**,**g**, Representative CLSM images of fluorescent sections of CT26 tumours in different groups showing immunogenic cell death (**f**) and cell apoptosis and proliferation (**g**). **h**, ELISA suggested that **1**-sensitized RT effectively increased extracellular levels of HMGB1 in tumour tissues (*n* = 10). **i**, Relative intensity analysis of CLSM images indicated that **1** sensitized RT, inducing the increase in CRT in tumour tissues (Blank, *n* = 13; RT, *n* = 18; **1**, *n* = 14; **1** + RT, *n* = 19). **j**, Quantitative analysis of caspase-3 to Ki67 fluorescence intensity ratio (*n* = 9). **k**, Changes in concentration of ATP in CT26 cells (*n* = 6). **l**, Relative intensity analysis of CLSM images indicated that **1** sensitized RT, inducing the increase in γH2AX in CT26 tumour tissues (*n* = 16). **m**, Representative CLSM images of fluorescent sections of CT26 tumours in different groups showed the expression of γH2AX in the nucleus. **n**, Schematic illustration showing that **1** produced platinonitrene upon RT and induced cell death. **o**–**q**, Comet assay: representative images (**o**), DNA damage grading (**p**) and Tail DNA% (**q**; Blank, *n* = 69; RT, *n* = 66; **1**, *n* = 62; **1** + RT, *n* = 64), with **1** + RT showing maximal damage. **r**, Representative images of clonogenic assay. **s**, Survival fraction of different doses showing that complex **1** could effectively sensitize RT (*n* = 3). Boxplots: centre line, median (50th percentile); box bounds, 25th–75th percentiles (interquartile range (IQR)); whiskers, min/max within 1.5× IQR. The Mann‒Whitney test was used for two-group comparisons. One-way ANOVA with Tukey's multiple comparisons test was used when more than two groups were compared. Data presented as mean ± s.d., and all replicates are independent biological samples.

expression of Ki67 in the other groups was relatively higher, and only the RT group showed some signal of caspase-3, which suggests that RT alone may not be sufficient to effectively inhibit tumour growth (Fig. 2j). Moreover, **1** in combination with RT effectively elevated adenosine triphosphate (ATP) production by 1.5-fold compared to the control group (Fig. 2k). Moreover, we found that **1**-sensitized RT could effectively promote DNA damage, and the expression of γH2AX in tumour tissues was notably increased (Fig. 2l,m and Supplementary Fig.11). In the comet assay, CT26 cells in the **1** + RT group exhibited a distinct comet trailing phenomenon with the highest tail DNA content (Fig. 2o–q and Supplementary Fig.12), indicating that **1**-sensitized RT effectively induced DNA fragmentation. Clonogenic assay confirmed that **1** could significantly enhance the killing effect of RT (Fig. 2r,s and Supplementary Fig.13). These results suggest that much more robust ICD and DNA damage were also evoked by **1** sensitization (Fig. 2n), which would elicit immune responses[2,30] and had the potential to enhance the abscopal effect.

Complex 1 exerts potent antitumoural responses when treated with RT

We further investigated whether **1** could sensitize RT in vivo and inhibit tumour growth in a mouse colon cancer model, with CT26 cells being injected subcutaneously[32] (Fig. 3a and Supplementary Fig. 14). Tumour growth rate in the **1** + RT group was much slower than those in the other treatments. In contrast, tumour progression in the **1**-alone group was similar to that in the control group, indicating that **1** itself without RT does not have any antitumour effect (Fig. 3b,c). Based on survival analysis, **1** + RT was able to notably prolong the survival time of CT26 tumour-bearing mice, with ~1/3 of the mice being completely cured. Survival in the **1**-alone group was also similar to that in the control group (Fig. 3d), suggesting that **1** sensitized RT and inhibited tumour growth only upon radiation (Fig. 3e). We also studied the antitumour efficacy of **1**-sensitizing RT in triple-negative breast cancer mice bearing 4T1 tumour (Extended Data Fig. 2a), which showed similar trends (Extended Data Fig. 2b–d). In addition, the lungs of 4T1 tumour-bearing mice were collected and lung nodules were counted, which demonstrated that the number of metastasis nodules in the **1** + RT group was substantially less than those in the other groups (Extended Data Fig. 2e,f), suggesting that **1**-sensitized RT inhibited lung metastasis of 4T1 tumours. The above results suggest that sensitization of **1** to RT displayed more potent antitumour efficacy. Another platinum-based azido compound, *cis*-$\text{Pt(NH}_3)_2(\text{N}_3)_2$, also showed excellent sensitization to RT (Extended Data Fig. 3).

T cells, especially CD8$^+$ T cells, hold an essential role in antitumour immune responses, and they need to be activated by mature dendritic cells (DCs) to possess tumour-killing ability[33]. We investigated the maturation of DCs with different treatments. Tumour-draining lymph nodes (TDLNs) were collected after dosing, followed by flow cytometry analysis. Treatment with **1** + RT induced the highest percentage of CD80$^+$CD86$^+$ DCs, which was 2 to 3 times higher than that in the control group as well as the RT group (Fig. 3f), suggesting that the **1**-sensitized RT treatment was able to promote the maturation of DCs in the TDLNs in comparison to treatment with RT only. Meanwhile, consistent with the trends in tumour growth data, tumours isolated from animals treated with **1** + RT were much smaller and had a considerably higher proportion of CD45$^+$CD3$^+$ T cells infiltrating the tumours, reaching twice the proportion of the other groups (Fig. 3g). Moreover, the mean proportion of cytotoxic CD8$^+$ T lymphocytes in tumours treated with **1** + RT increased by ~50% of those found in the other groups (Fig. 3h). Surprisingly, the proportion of regulatory T cells (Tregs) in tumours treated with **1** + RT was substantially reduced, with an average proportion of only ~16% of those found in the control and RT groups (Fig. 3i). The same phenomenon was also observed in the **1**-only group, which indicated that **1** itself had the effect of inhibiting the infiltration of Tregs. The investigation on the killing ability of intratumoural CD8$^+$ T cells showed that **1**-sensitized RT significantly increased the proportion of CD8$^+$IFNγ$^+$, CD8$^+$CD107a$^+$ and CD8$^+$PD1$^+$TIM3$^+$ T cells (Fig. 3j–l). In addition, the intratumoural content analysis of IFNγ and Granzyme B showed that the **1** + RT group had the highest

Fig. 3 | Complex 1-sensitized RT effectively inhibits the growth of established CT26 tumours. a, Schemes of CT26 tumour inoculation, therapies and flow cytometry analysis. RT was initiated at a tumour size of ~120 mm (ref. 3). i.t., intratumoural injection. **b**, Tumour growth curves of each mouse. **c**, Average tumour growth curves showed that **1**-sensitized RT effectively inhibited the growth of established CT26 tumours (Blank and **1**, *n* = 8; RT and **1** + RT, *n* = 9). Tumour growth over time was compared by two-way ANOVA with Tukey's test. **d**, Survival curves showed that **1**-sensitized RT prolonged the survival time of mice (Blank and **1**, *n* = 8; RT and **1** + RT, *n* = 9). Differences in survival were determined for each group using the Kaplan–Meier method, and the overall *P* value was calculated using the log-rank test. **e**, Tumour weight in different groups at day 18 (Blank, RT and **1**, *n* = 6; **1** + RT, *n* = 12). **f**, Quantification of DC maturation in TDLNs by flow cytometry indicated that **1**-sensitized RT induced the highest percentage of CD80$^+$CD86$^+$ DCs (Blank, *n* = 8; **1**, *n* = 7; RT and **1** + RT, *n* = 9). **g**–**i**, Quantification of tumour-infiltrating CD45$^+$CD3$^+$, CD8$^+$ and Treg (CD4$^+$Foxp3$^+$) cells by flow cytometry (Blank, *n* = 8; **1**, *n* = 7; RT and **1** + RT, *n* = 9). **j**–**l**, Quantification of tumour-infiltrating CD8$^+$IFNγ$^+$, CD8$^+$CD107a$^+$ and CD8$^+$PD1$^+$TIM3$^+$ T cells by flow cytometry (*n* = 6). **m**,**n**, Results of ELISA suggested that **1**-sensitized RT effectively increased secretion of IFNγ and Granzyme B in tumour tissues (*n* = 10). **o**, GSEA indicated that **1**-sensitized RT improved the responsiveness of PD-L1 expression and the PD-1 checkpoint pathway. **p**, Changes in expression levels of representative genes in PD-L1 expression and PD-1 checkpoint pathway in cancer. The Mann‒Whitney test was used for two-group comparisons. One-way ANOVA with Tukey's multiple comparisons test was used when more than two groups were compared. Data are presented as mean ± s.d., and all replicates are independent biological samples.

content (Fig. 3m,n). Gene set enrichment analysis (GSEA) showed that **1**-sensitized RT improved the responsiveness of PD-L1 expression and the PD-1 checkpoint pathway. The expression levels of the main related genes were also significantly increased (Fig. 3o,p). This suggests a potential advantage in combination with PD-1 pathway checkpoint inhibitors.

We investigated the mechanism at the genetic level with RNA sequencing (RNA-seq) analysis of tumour tissues after treatment.

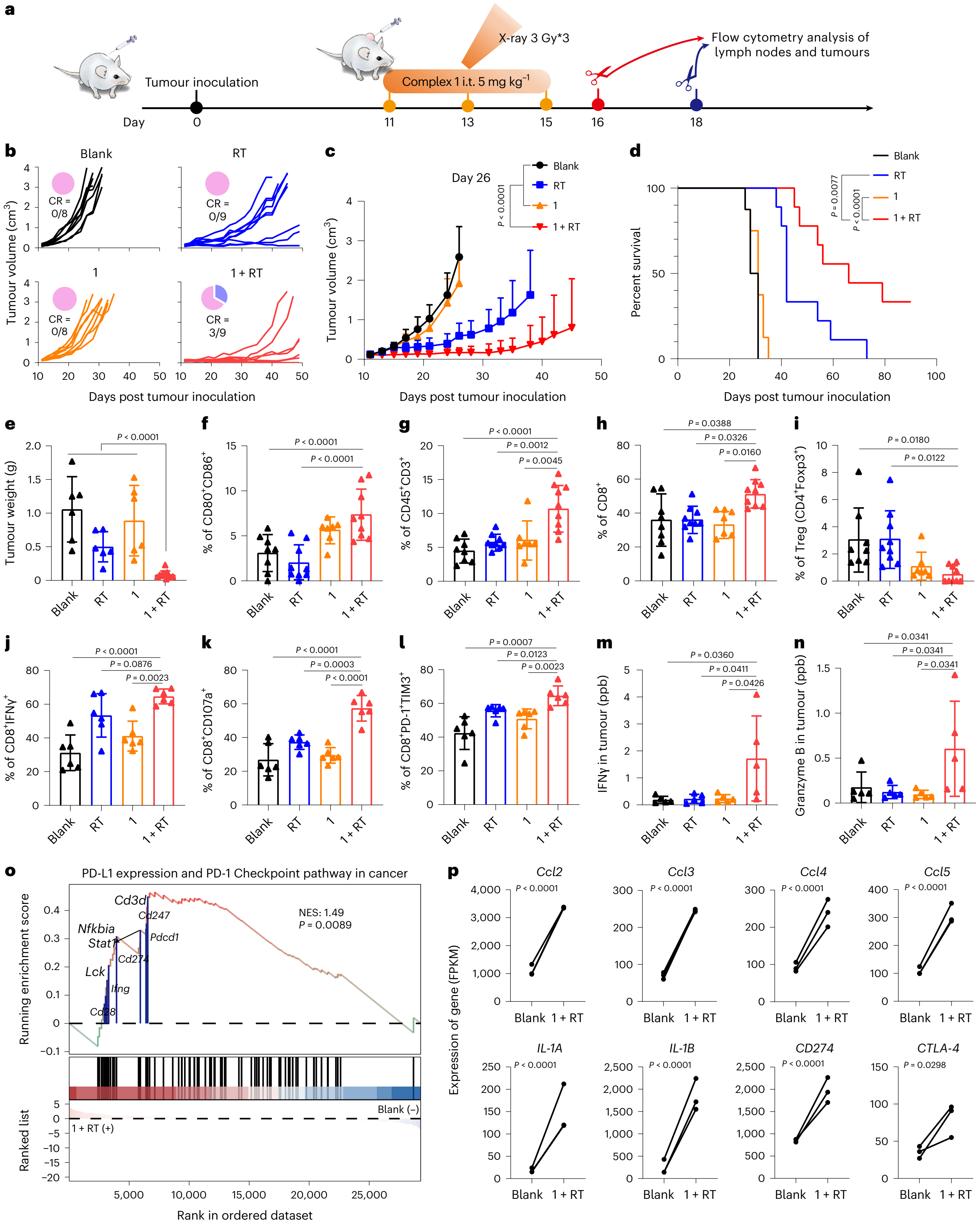

Principal component analysis (PCA) showed some variabilities among different treatments (Fig. 4a). The tumour microenvironment (TME) was scored using the Estimation of STromal and Immune cells in MAlignant Tumour tissues using Expression data (ESTIMATE) algorithm. The results showed that the **1** + RT group had higher stromal score (Fig. 4b) and immune score (Fig. 4c), indicating that **1**-sensitized RT could promote the infiltration of immune cells into the TME. Meanwhile, the ESTIMATE score was considerably higher (Fig. 4d), and tumour purity was notably lower in the **1** + RT group (Fig. 4e), indicating that the proportion of tumour cells in the tumour tissues decreased, and the non-tumour cell components increased after the **1** + RT treatment. Through differential gene clustering analysis, we found that **1**-sensitized RT was able to promote the expression of many immune-related signalling pathway genes, including genes of the innate immune response-related pathways and inflammatory response-related pathways (Fig. 4f–i and Supplementary Figs. 15–17), denoting that **1**-derived radiosensitization not only leads to direct DNA damage but also promotes activation of the immune response through multiple pathways. The proportion of tumour-killing immune cells, such as activated CD8$^+$ T cells, was notably increased in the **1** + RT group (Fig. 4j), and CIBERSORT revealed a substantial decrease in the proportion of tumour-infiltrating Tregs (Supplementary Fig. 18), which corresponded with the flow cytometry analysis (Fig. 3i).

Noting the potential inhibitory effect of **1** on Treg cells, we further investigated this in several aspects. We studied the phenotype of major immune cells (such as CD4$^+$, CD8$^+$, Treg cells, myeloid-derived suppressor cells (MDSC) and tumour-associated macrophage (TAM); Supplementary Figs. 19–21) and the expression of molecules related to Treg (such as GITR, Helicos, ICOS and Nrp-1; Supplementary Figs. 22–24), function and activation of Treg (such as CD39, CD44, CD69 and PD-1; Supplementary Figs. 25–27) and killing capacity of CD8$^+$ T cells (Supplementary Figs. 28 and 29) in tumour, spleen and draining lymph node. Results implied that **1** did not inhibit Treg infiltration primarily through the immune response. Splenic T cells isolated from BALB/c mice were co-incubated with **1**, followed by RT (Fig. 5a). We found that RT had a significant killing effect on all T cell subpopulations, and that **1** itself could inhibit the proliferation of splenic T cells, especially Treg cells, either combined with RT or not (Fig. 5b–f). Therefore, we further explored the effect of **1** itself on T cell proliferation using carboxyfluorescein diacetate succinimidyl ester (CFSE)-stained splenic T cells isolated from C57BL/6-Foxp3^{tm1Flv}/J mice (Fig. 5g). To exclude the effect of apoptosis on cell proliferation due to the cytotoxicity of **1** itself, we set up different gradient concentrations and found that Treg cells were able to proliferate normally when the concentration of **1** was <1.0 μg ml^{-1}. The proliferation of Treg cells was significantly inhibited when the concentration reached 2.0 μg ml^{-1} (Fig. 5h). Moreover, we found that Treg cells were able to remain active with no significant increase in apoptosis when concentration was lower than 2.0 μg ml^{-1} (Fig. 5i–k). This suggests that **1** itself has the ability to inhibit Treg cell proliferation rather than via induction of Treg cell apoptosis. In addition, CD4$^+$ and CD8$^+$ T cells were still able to proliferate normally when the complex **1** concentration reached 2.0 μg ml^{-1} (Fig. 5i). Complex **1** exhibited stronger selective inhibition against Treg cell proliferation compared with CD4$^+$ and CD8$^+$ T cell proliferation (Fig. 5l,m,n). Together, the above results suggest that **1** could act as a radiosensitizer to enhance the effect of RT and promote the activation of immune responses.

Sensitization of complex 1 to a low dose of RT enhanced the abscopal effect

Based on the above results, **1** might hold a role in immunity while sensitizing radiotherapy, so we investigated whether it could improve the efficacy of immune checkpoint blockade. We first investigated **1** sensitization to RT at low dose combining αPD-1 to treat mice bearing a single established CT26 tumour, and we found that low-dose RT combined with αPD-1 has limited efficacy. With sensitization of **1** to RT, αPD-1 therapeutic efficacy was notably enhanced (Fig. 6a and Supplementary Fig. 30), which suggests that the enhancement required sensitization of **1**. As shown in Fig. 6b, the survival time in the **1** + RT + αPD-1 group was substantially longer, with 20% of mice completely cured, indicating that platinonitrene induced by RT as intermediate sensitized RT to enhance αPD-1 immunotherapy.

We further assessed whether this activation could be expanded to systemic responses. To evaluate the hypothesized systemic responses derived from **1**-sensitized RT with combined αPD-1 therapy, a bilateral CT26 tumour model was applied to evaluate the abscopal effect. The primary tumours received low-dose RT combined with **1** intratumourally (i.t.), while αPD-1 was given at the same time (Fig. 6c and Supplementary Fig. 31). The growth rates of both primary (Fig. 6d,e) and secondary tumours (Fig. 6d,f) in the **1** + RT + αPD-1 group were much slower, whereas low-dose RT in combination with αPD-1 was unable to achieve effective inhibition of primary and secondary tumours in the absence of sensitizer **1**. In addition, low-dose RT combined with sensitizer **1** as well as αPD-1 notably prolonged the survival time, and ~40% of mice were completely cured with regression of bilateral tumours (Fig. 6g and Extended Data Fig. 4). We collected both in situ and distal tumours and analysed T-cell infiltration. The proportion of CD45$^+$CD3$^+$ T cells was considerably elevated in both in situ and distal tumours in the **1** + RT + αPD-1 group (Fig. 6h), while the proportion of CD8$^+$ T cells was markedly increased in primary tumours (Fig. 6i). Encouragingly, the proportions of Tregs were considerably decreased in both primary and secondary tumours (Fig. 6j), which coincided with the previous flow cytometry analysis and RNA-seq results of the single tumour model. Traditional RT has the effect of upregulating the infiltration of suppressive immune cells and directly damaging circulating lymphocytes[4], including CD8$^+$ T cells. However, we found notable increases in the ratios of CD8$^+$/Tregs and CD4$^+$/Tregs in both primary and secondary tumours in the **1** + RT + αPD-1 group (Fig. 6k,l and Extended Data Fig. 5). These suggested that the immune-activating effects of **1**-based radio-immunotherapy far exceeded the immunosuppressive effect. In addition, the proportion of CD80$^+$CD86$^+$ DCs in the draining lymph nodes near the irradiated primary tumours in the **1** + RT + αPD-1 group was also much higher (Extended Data Fig. 5), confirming the activation of adaptive immune responses.

Fig. 4 | RNA-seq of CT26 tumour tissues suggests that complex 1-sensitized RT induced immune cell infiltration into the TME. a, PCA of each group ($n = 3$). **b**–**e**, TME score based on ESTIMATE indicated that **1**-sensitized RT could promote the infiltration of immune cells ($n = 3$). **f**, Hierarchical clustering and heat map of differentially expressed genes among four groups based on RNA-seq data. Each row represents a transcript, and each column represents the average expression level of a sample group. Hierarchical clustering results are indicated by different colours. DEseq2 was used for differential gene expression analysis, and data were normalized using *z*-scores. The significance threshold for differential expression was set at $P_{adj} < 0.05$ and logFC > 2 ($n = 3$). **g**, GO terms for high-scoring genes within each cluster corresponding to **f**. Gene annotation was performed using Metascape. Colours represent the groupings of genes, and values represent $-\log_{10}$ (*P* value). **h**, Chordal plot demonstrating differential genes between Blank and **1** + RT group enrichment in immune response-related KEGG terms ($n = 3$). **i**, GSEA analysis indicated that **1**-sensitized RT improved the responsiveness of representative immune-related pathways ($n = 3$). FDR, false discovery rate. **j**, Analysis of tumour-infiltrating immune cells based on single-sample GSEA indicated that **1**-sensitized RT could increase the proportion of tumour-killing immune cells ($n = 3$). Values were scaled to the [0, 1] interval using min/max normalization. One-way ANOVA with Tukey's multiple comparisons test was used when more than two groups were compared. Data are presented as mean ± s.d., and all replicates are independent biological samples.

Sensitization of 1 to RT shows reliable biosafety and immune memory effect

We investigated the biosafety of **1** as sensitizer for RT, with mice being systemically administered with **1** via the tail veins. Unlike oxaliplatin (OXP), **1** alone did not display any antitumour efficacy, whereas when used as a radiosensitizer, it notably inhibited tumour growth (Fig. 7a and Supplementary Fig. 32). Moreover, the OXP + RT treatment was unable to prolong the survival of mice compared to RT alone, whereas

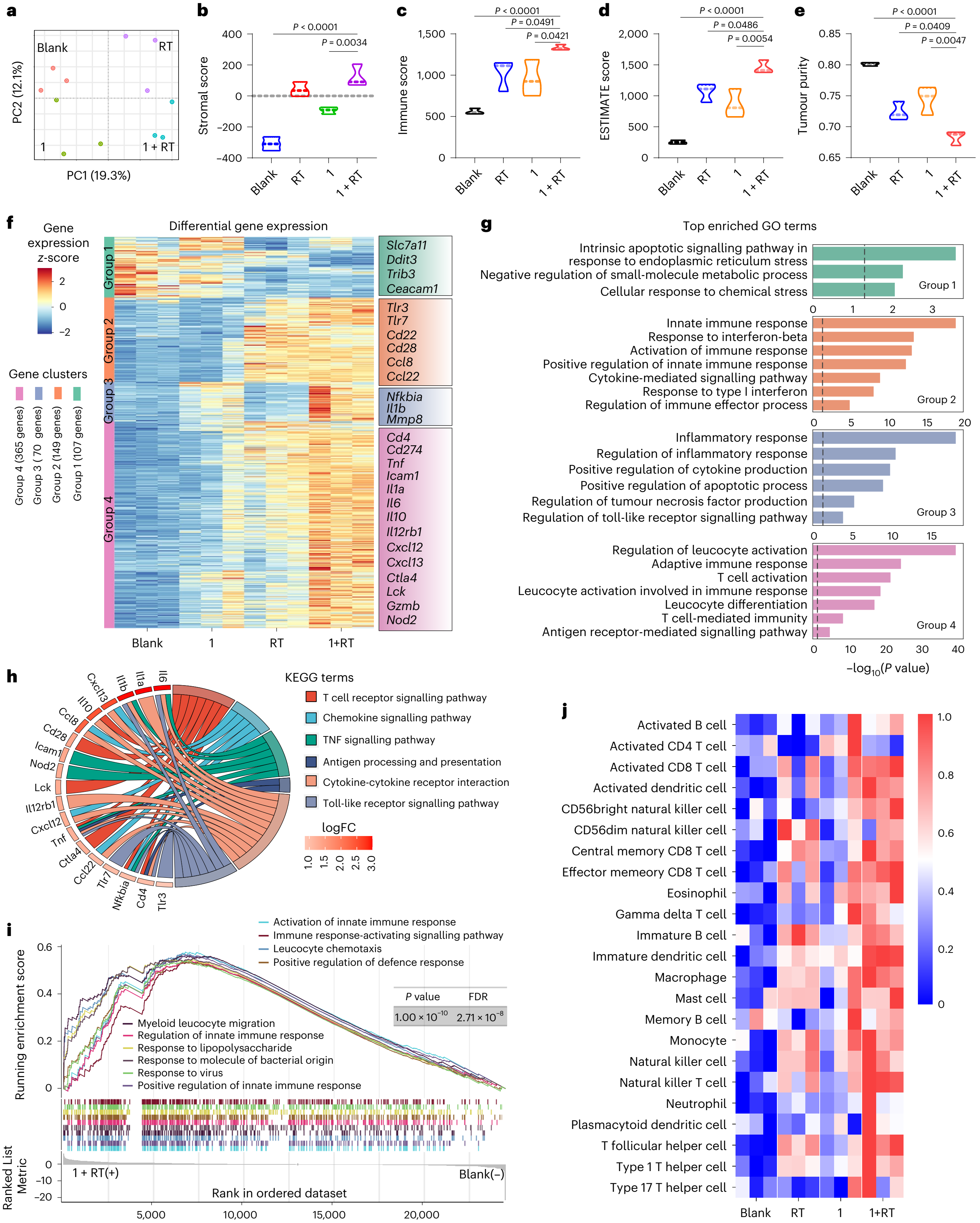

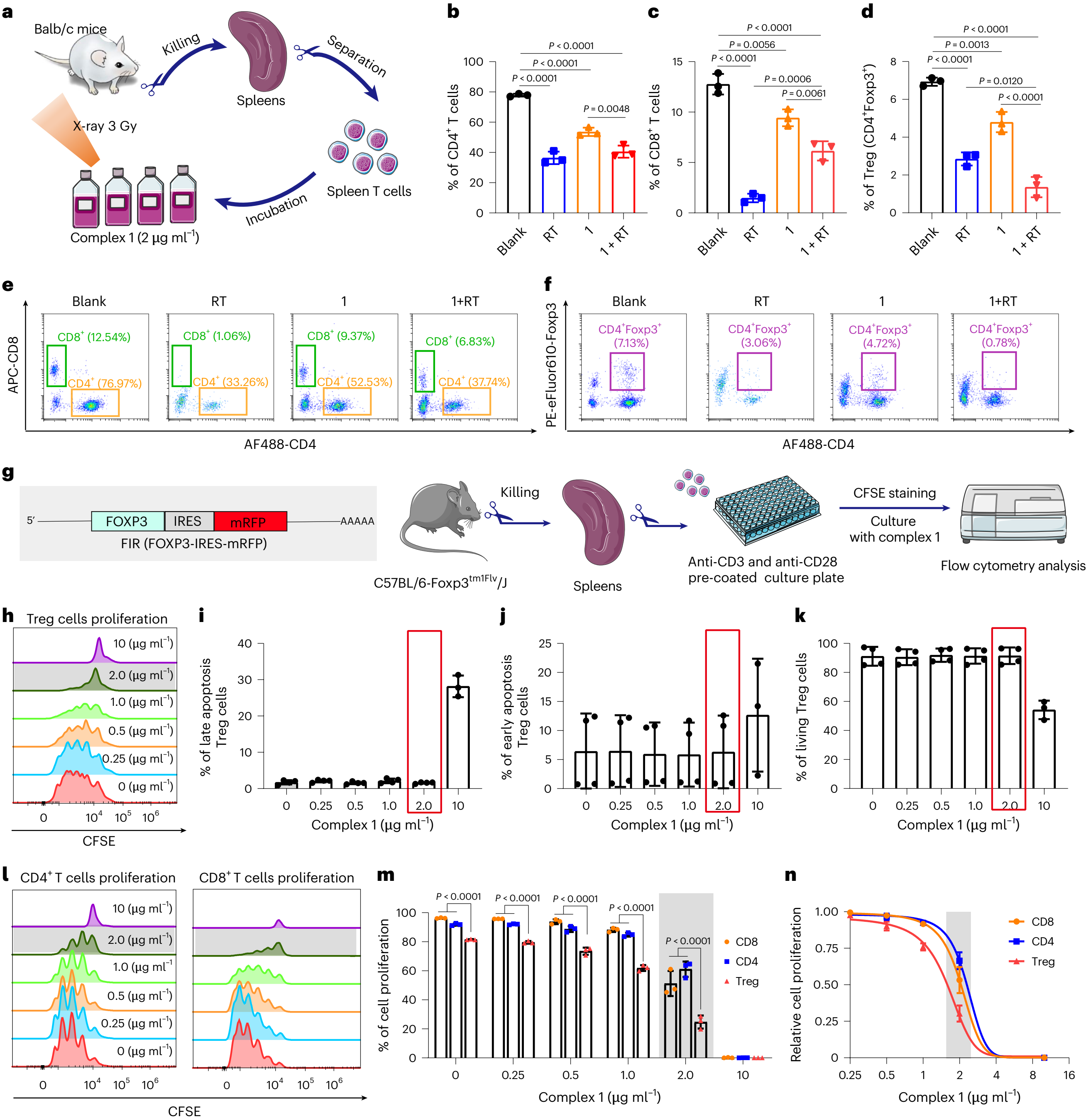

Fig. 5 | Complex 1 itself could inhibit Treg cell proliferation. a, Scheme of spleen isolation from BALB/c mice for experiments. **b**–**d**, Quantification of splenic T cells cultured ex vivo after different treatments, by flow cytometry ($n = 3$). **e**,**f**, Corresponding representative flow cytometry plots showing the proportion of CD4$^+$, CD8$^+$ and Treg cells. **g**, Splenic T cells isolated from C57BL/6-Foxp3$^{\mathrm{tm1Flv}}$/J mice were cultured and stained with CFSE to study cell proliferation. **h**, Representative flow cytometry plots showing the effect of different concentrations of complex **1** on Treg cell proliferation ($n = 3$). **i**–**k**, Effect of different concentrations of complex **1** on Treg cell apoptosis ($n = 4$, except for 10 μg ml^{-1}, $n = 3$). **l**, Representative flow cytometry plots showing the effect of different concentrations of complex **1** on CD4$^+$ and CD8$^+$ T cell proliferation. **m**,**n**, Effect of complex **1** on the proliferation ratio of CD4$^+$, CD8$^+$ and Treg cells, indicating that **1** had a stronger selective inhibitory effect on the proliferation of Treg cells ($n = 3$). One-way ANOVA with Tukey's multiple comparisons test was used when more than two groups were compared. Data are presented as mean ± s.d., and all replicates are independent biological samples.

sensitization with **1** considerably prolonged survival in the **1** + RT group. About 70% of mice achieved complete tumour regression (Fig. 7b). This suggested that the azido moiety of **1** conferred it with an entirely different property. The produced platinonitrene under RT bonded to DNA by N-N coupling (Pt-N-N-DNA) and further sensitized RT, superior to the effect of oxaliplatin.

Pathologic sections (Fig. 7c and Supplementary Fig. 33) showed that **1** did not cause obvious damage to main organs. The kidney of

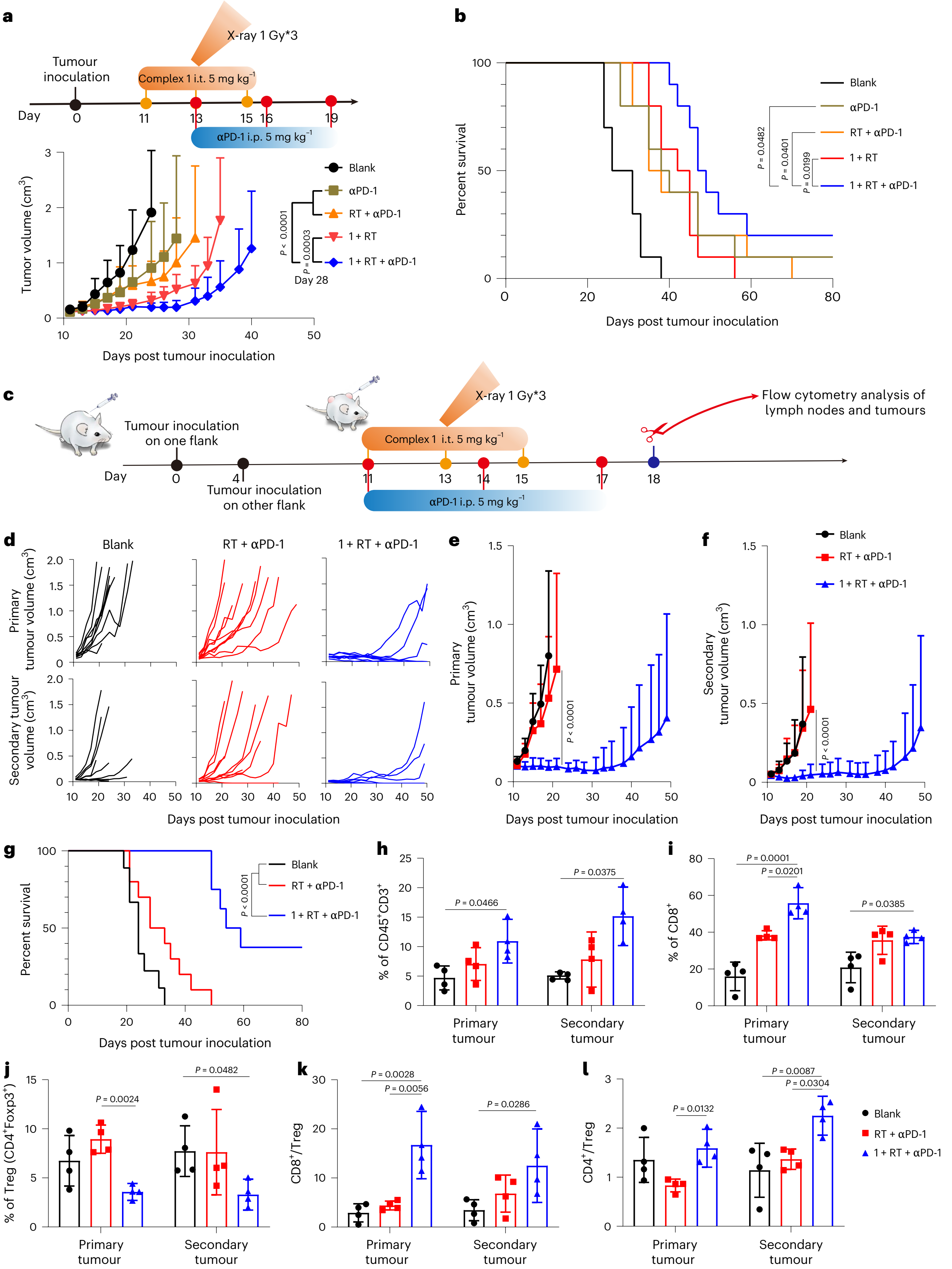

mice treated with oxaliplatin exhibited more inflammatory cell infiltration as well as apoptosis (Fig. 7c). There was an increase in creatinine (CRE) and blood urea nitrogen (BUN) proportion in peripheral blood (Fig. 7d,e). We also compared the antitumour efficacy and biosafety of oxaliplatin versus **1** combined with low-dose RT and αPD-1 in a bilateral tumour model (Extended Data Fig. 6). Sensitization of **1** to RT could also improve the abscopal effect more effectively than that of oxaliplatin, without causing renal injury or hepatitis[34–36].

Fig. 6 | Complex 1-sensitized RT enhances immunotherapy and the abscopal effect on syngeneic CT26 tumour model. a, Average tumour growth curves showing that **1** combined with a low dose of RT improved αPD-1 therapy ($n = 10$). **b**, Survival curves showing that **1** combined with a low dose of RT and αPD-1 prolonged survival time of mice ($n = 10$). **c**, Schemes of primary and secondary tumour inoculation, therapies and flow cytometry analysis in the study of the abscopal effect. **d**, Primary and secondary tumour growth curves of each mouse showing that **1** in combination with RT and αPD-1 suppresses growth of bilateral tumours (Blank, $n = 9$; RT + αPD-1, $n = 10$; **1** + RT + αPD-1, $n = 8$). **e**, Average primary tumour growth curves of each group (Blank, $n = 9$; RT + αPD-1, $n = 10$; **1** + RT + αPD-1, $n = 8$). **f**, Average secondary tumour growth curves of each group (Blank, $n = 9$; RT + αPD-1, $n = 10$; **1** + RT + αPD-1, $n = 8$). Tumour growth over time was compared using two-way ANOVA with Tukey's test. **g**, Survival curves showing that **1** in combination with RT and αPD-1 prolonged survival time of mice in bilateral tumour model (Blank, $n = 9$; RT + αPD-1, $n = 10$; **1** + RT + αPD-1, $n = 8$). Differences in survival were determined for each group using the Kaplan–Meier method, and the overall P value was calculated using the log-rank test. **h**–**j**, Quantification of primary and secondary tumour-infiltrating $CD45^+CD3^+$, $CD8^+$and Treg ($CD4^+Foxp3^+$) cells by flow cytometry ($n = 4$). **k**,**l**, Ratios of $CD8^+$ cells to Treg cells and $CD4^+$ cells to Tregs based on flow cytometry analysis were increased after **1** sensitized RT with αPD-1 ($n = 4$). One-way ANOVA with Tukey's multiple comparisons test was used when more than two groups were compared. Data are presented as mean ± s.d., and replicates are independent biological samples.

In addition, we further investigated whether the **1**-derived cure of mice established durable and potent immune memory effects (Fig. 7f). Flow cytometry analysis of peripheral blood showed that the proportion of $CD44^+CD62L^-$ effector memory T cells in cured mice was much higher than that in the naïve group (Fig. 7g,h and Supplementary Fig. 34). We further performed tumour rechallenge of mice whose tumours had completely regressed for more than 250 days, and the mice were still able to continue to remain free from re-invasion by the same type of tumour (except for one mouse that died naturally because of age) (Fig. 7i,j). Thereafter, the third tumour inoculation was applied to the re-cured mice 2 months later, and all the re-cured mice were still able to continue to reject tumour growth and were cured for the third time (Fig. 7k,l and Supplementary Fig. 35). This demonstrated that **1**-sensitized RT was able to establish a long-lasting and robust immune memory effect in vivo. In addition, we investigated the manner by which complex **1** entered into cells in vitro (Supplementary Fig. 36) and the biological distribution of complex **1** in vivo. We found that **1** was also able to enter the brain (Supplementary Fig. 37 and 38), and **1**-sensitized RT could also inhibit the growth of orthotopic glioblastoma (Extended Data Fig. 7).

Discussion

RT exerts antitumour effects primarily directly by damaging DNA, or by cleaving water molecules to generate ROS and free radicals, ultimately inducing DNA damage indirectly. Many radiosensitizers are designed on the basis of this principle and several of them are already used in the clinic or in clinic trials with promising therapeutic outcomes. However, current radiosensitizers are administered either before or after RT and could display off-target effects and adverse effects without radiation. They also lack tumour specificity. These drawbacks hinder their clinical translation. Thus, the development of a radiosensitizer that can sensitize RT upon low-dose radiation is a major need. In other words, radiation-derived generation of toxic substances from the radiolysis of the sensitizer not only addresses the limitations of classic radiosensitizers but could also minimize systemic toxicity, preserve the efficacy of sensitization and promote tumour regression.

Metallonitrene is a highly reactive intermediate that has strong ability to attract electrons. The developed complex **1** here displayed negligible systemic toxicity except for inhibiting tumour infiltration of Treg cells without radiolysis, while it can generate platinonitrene with a low dose of RT and attack the amine group of cytosine base on DNA, resulting in N-N coupling between complex **1** and DNA. The DNA binding process is different from the classic mechanism of platinum-based drugs, which directly form a Pt-N coordinated structure with DNA. These results provide different aspects for metallodrug design, especially for platinum-based drugs.

Cancer stem cell (CSC)-associated radioresistance and the extent of hypoxia in tumour tissue that affects radiosensitivity will decrease the outcome of RT[37,38]. CSCs have the ability for self-renewal and differentiation, and they may re-form tumour tissues after RT. RT could more effectively eradicate fast-dividing and proliferating tumour cells, and CSCs are usually quiescent or dormant, thereby resisting the killing effect of RT. In addition, subsets of CSCs in some tumours that have lower ROS levels might also contribute to radioresistance. ROS inducers for the radiosensitization strategy have been widely investigated. However, the defence network of hypoxic cancer cells could effectively detoxify ROS, which may make them induce hypoxic radioresistance. Different from classic radiosensitizers that maximize ROS generation to boost radiotherapy, our sensitization does not depend on ROS production. It sensitizes radiotherapy via DNA damage with metallonitrene.

In summary, we have developed a platinum complex **1** and found that it could produce highly reactive platinonitrene in vivo only upon exposure to RT, further reacting with bases of DNA by N-N coupling (Pt-N-N-DNA) to form stable chemical bonds, which in turn enhance DNA damage post RT. Thereby, it sensitized RT to effectively inhibit tumour growth independent of ROS. The enhanced DNA damage on irradiated primary tumour reshaped the tumour microenvironment and elicited stronger immune responses, while **1** itself did not show obvious systemic toxicity except for inhibiting the intratumoural infiltration of Tregs. Therefore, **1**-sensitized RT could effectively improve the efficacy of ICIs and induce the abscopal effect by up to 40%, an improvement not seen before.

Fig. 7 | Complex 1-sensitized RT has reliable biosecurity and derives long-lasting immune memory effect on syngeneic CT26 tumour model. a, Average tumour growth curves showing **1**-sensitized radiotherapy suppressing tumour growth more effectively than oxaliplatin (Blank, RT and **1**, $n = 6$; OXP, OXP + RT and **1** + RT, $n = 7$). RT was initiated at a tumour size of ~70mm^3. i.v., intravenous injection. **b**, Survival curves showing **1**-sensitized radiotherapy significantly prolonging the survival time of mice compared with oxaliplatin (Blank, RT and **1**, $n = 6$; OXP, OXP + RT and **1** + RT, $n = 7$). **c**, Representative TdT-mediated dUTP nick-end labelling (TUNEL) and haematoxylin and eosin (H&E) staining sections of kidney showing that **1** had less neurotoxicity than oxaliplatin. Red arrow, apoptotic cells; red box, inflammatory cell infiltration. **d**,**e**, CRE and BUN analysis in serum showing that **1** would cause negligible liver damage ($n = 9$). NS, not significant. **f**, Scheme of tumour rechallenge for cured mice. **g**,**h**, Representative flow cytometry plots and quantitative histogram showing that cured mice held a higher proportion of $CD44^+CD62L^-$ effector memory T cells ($n = 10$). **i**,**j**, Average tumour growth curves and survival curves showing that cured mice could cure again (except one mouse that died naturally because of age) ($n = 10$). **k**,**l**, Average tumour growth curves and survival curves showing that twice-cured mice were able to resist the third round of tumour inoculation (Naïve group, $n = 10$; twice-cured group, $n = 9$). Tumour growth over time was compared using two-way ANOVA with Tukey's test. Differences in survival of the groups were determined using the Kaplan–Meier method, and the overall P value was calculated using the log-rank test. One-way ANOVA with Tukey's multiple comparisons test was used when more than two groups were compared. Data are presented as mean ± s.d., and all replicates are independent biological samples.

Outlook

Our findings here bring metallonitrene from in vitro coupling in organic chemistry to in vivo application for drug discovery, providing proof of concept of radiosensitization with metallonitrene. We used a low dose of high-energy rays to accurately produce highly reactive platinonitrene in situ that could enhance DNA damage intratumourally, which would lead to safer and more affordable treatment regimens. This local activation strategy to release highly active species to damage tumour DNA also provides a different mechanism for metal drug design. Our work potentially promises a chemistry strategy for

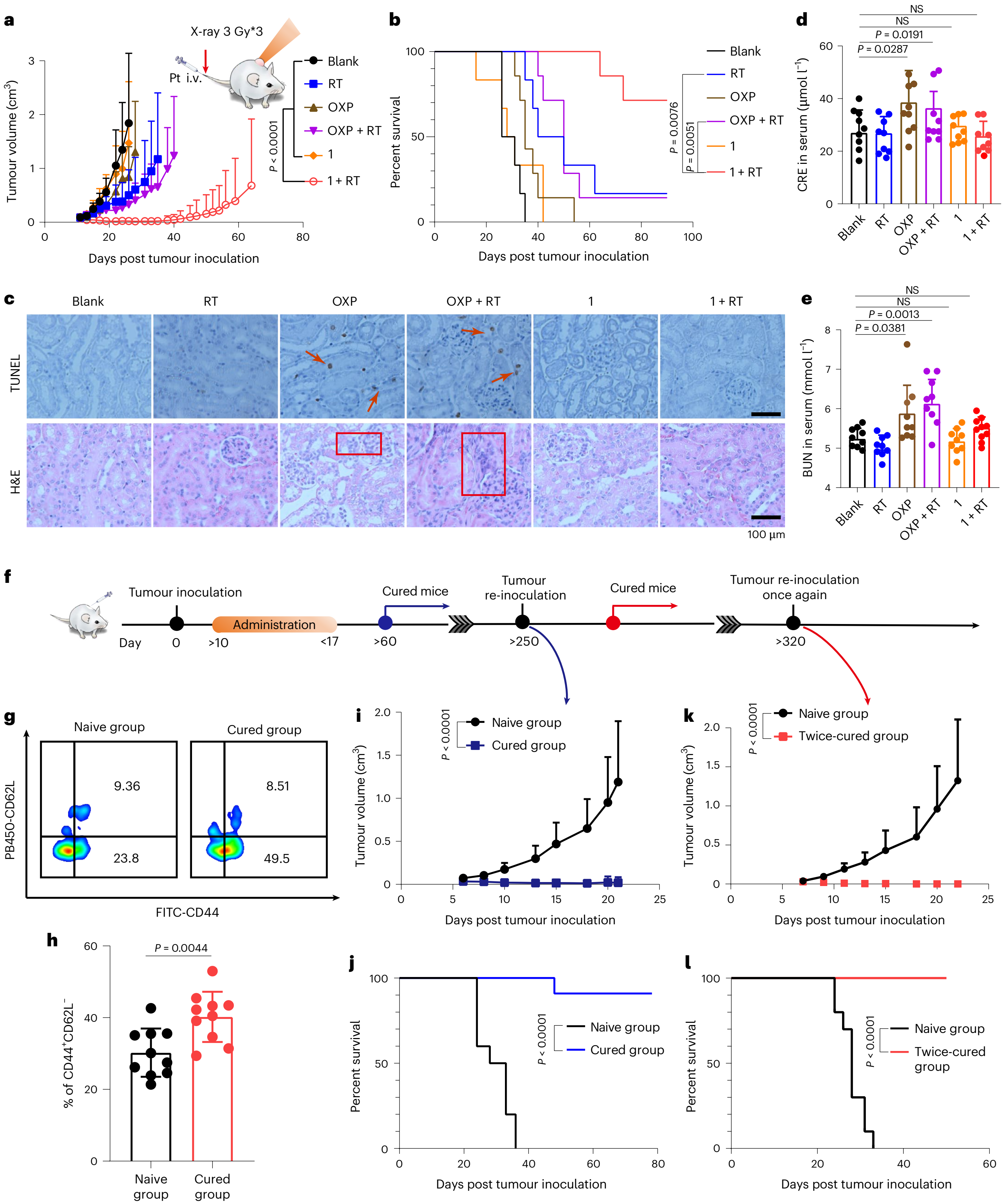

developing radiosensitizers, promoting the development of precision and translational medicine.

Methods

Materials

K_2PtCl_4, cisplatin and oxaliplatin were purchased from Boyuan Pharmaceutical. Except for those specifically mentioned, all other compounds were purchased from Sinopharm and Bidepharm.

Superoxide Anion Assay kits (BL880A) were purchased from Biosharp, and Mitochondrial Membrane Potential Assay kit with Rhodamine 123 (C2008S), mouse IFNγ ELISA kit (PI508) and Enhanced ATP Assay kit (S0027) were purchased from Beyotime. The MojoSort mouse CD4 T Cell Isolation kit (408033, B386335) was purchased from Biolegend. Mouse Granzyme B (GzmB) ELISA kit (D721076-0096) and mouse HMGB1 ELISA kit (SEKM-0145) were purchased from Sangon Biotech and Solarbio, respectively. Antibodies of HMGB1 (clone EPR3507, ab79823, GR3299518-1), CRT (clone EPR3924, ab2907, GR3333461-4) and Ki67 (clone SP6, ab16667, GR227625-4) used for immunofluorescence were all bought from Abcam, and antibodies of caspase-3 (clone AMC0214, 19677-1-AP, 00088666) were bought from Proteintech. Antibodies of CD3 (clone 145-2C11, 480033, B386335) and CD28 (clone 37.51, 102116, B351568) were purchased from Biolegend. Recombinant human TGF-β1 (781802, B311005) and recombinant human IL-2 (200-02) were bought from Biolegend and Peprotech, respectively. Fluorescent antibodies used for flow cytometry include: anti-mouse CD45-eFluor 450 (clone. 30-F11, 48-0451-82, 228168), anti-mouse CD3-APC-eFluor 780 (clone 17A2, 47-0032-82, 2325387), anti-mouse CD4-Alexa Fluor 488 (clone RM4-5, 557667, 1096426), anti-mouse CD8α-APC (clone 53-6.7, 17-0081-82, 2356251), anti-mouse Foxp3-PE-eFluor 610 (clone FJK-16s, 61-5773-82, 2244811), anti-mouse CD11c-PE/Cy7 (clone N418, 558079, 1187822), anti-mouse CD80-BV421 (clone 19-10A1, 562611, 1256663), anti-mouse CD86-APC (clone GL1, 558079, 1308555), anti-mouse CD44-FITC (clone IM7, 11-0441-82, 2262273), anti-mouse CD62L-eFluor 450 (clone MEL-14, 48-0621-82, 2455897), anti-mouse Foxp3-PE (clone R16-715, 563101, 2175160), anti-mouse CD11b-PE-Cy7 (clone M1/70, 561098, B316177) and anti-mouse CD16/CD32 (clone 2.4G2, 553141, 1040760), purchased from Thermo Fisher and BD Bioscience. Anti-mouse CD45-PerCP/Cy5.5 (clone 30-F11, 103132, B385175), anti-mouse CD3-FITC (clone 145-2C11, 100306, B369904), anti-mouse CD8-PE/Cy7 (clone 53-6.7, 100722, B413191), anti-mouse CD107a-Brilliant Violet 421 (clone 1D4B, 121618, B360353), anti-mouse CD4-APC/Cy7 (clone RM4-5, 100526, B382617), anti-mouse IFNγ-APC (clone XMG1.2, 505810, B396246), anti-mouse PD1-PE (clone 29F.1A12, 135206, B383866), anti-mouse TIM3-APC (clone RMT3-23, 119706, B358301), anti-mouse CD39-PE/Cy7 (clone Duha59, 143806, B393317), anti-mouse CD44-Alexa Fluor 700 (clone NIM-R8, 156009, B370174), anti-mouse CD69-Brilliant Violet 605 (clone H1.2F3, 104529, B392965), anti-mouse PD1-APC (clone 29F.1A12, 135209, B399565), anti-mouse Nrp-1-Brilliant Violet 421 (clone 3E12, 145209, B379195), anti-mouse Helios-PE/Cy7 (clone 22F6, 137235, B358673), anti-mouse GITR-APC (clone DTA-1, 126311, B351356), anti-mouse ICOS- Alexa Fluor 700 (clone C398.4A, 313527, B348115), anti-mouse Ly6G-PE (clone 1A8, 127608, B388208), anti-mouse Ly6C-FITC (clone HK1.4, 128006, B368468), anti-mouse F4/80-APC (clone BM8, 13116, B379376) and anti-mouse CD64-Brilliant Violet 421 (clone X54-5/7.1, 139309, B422389) were all bought from Biolegend. All flow cytometry antibodies were diluted at the ratio of 1:100 following manufacturer instructions. Live/dead Fixable Yellow Dead Cell Staining kit (L34959, Life Technologies) and Zombie Aqua Fixable Viability kit (423102, B353077, Biolegend) were used for distinguishing live/dead cells in flow cytometry analysis. Foxp3/Transcription Factor Staining Buffer set (00-5521-00, 00-5523-00) used for intramembrane antigen staining, and eBioscience Annexin V Apoptosis Detection kit (88-805-74, BMS500FI-300) were bought from Thermo Fisher. CFSE cell division tracker kit (423801, B383180) was bought from Biolegend. Monoclonal antibody αPD-1 (clone RMP1-14, BE0146, 825822M1) was purchased from BioXcell.

Animals and cell lines

BALB/c mice (female, 6–8 weeks) and C57BL/6J mice (female, 6–8 weeks, body weight 20 g) were purchased from Slac Laboratory Animal. C57BL/6-Foxp3$^{\text{tm1Flv}}$/J mice (also known as: FOXP3-IRES-mRFP, FIR; this X-linked targeted knock-in strain co-marks cells expressing the Foxp3 gene with monomeric red fluorescent protein (mRFP). RFP expression faithfully marks gene expression in lymphocytes) were gifted by Prof. Zhu Shu of the University of Science and Technology of China. All mice were housed in specific-pathogen free (SPF) rated environments with light and dark switching every 12 h, and were provided with adequate food and water. All animal experiments were performed in accordance with the procedures approved by the China Experimental Animal Care Commission at the University of Science and Technology of China and complied with all relevant ethics regulations.

The CT26 cell line and 4T1 cell line were purchased from the Cell Bank of the Chinese Academy of Sciences (Shanghai, China) and were cultured in RPMI 1640 medium (Gibco) added with 10% fetal bovine serum (FBS, Gibco) and 1% penicillin/streptomycin (Gibco). The Gl261-luc cell line was purchased from Yuanjing Biotechnology and cultured in DMEM medium (Gibco) added with 10% FBS (Gibco) and 1% penicillin/streptomycin (Gibco). Cells were cultured with a constant 5% CO_2 at 37 °C.

Synthesis and characterization of 1

K_2PtCl_4 (207.5 mg, 0.5 mmol, 1.00 equiv.) and *trans*-1,2-cyclohexanediamine (62.7 mg, 0.55 mmol, 1.10 equiv.) were suspended in H_2O (20 ml). After stirring in the dark for 24 h at 40 °C in a glass flask, the state of the reaction system changed from a yellow transparent solution to a yellow turbid solution. The reaction system was centrifuged to discard the supernatant to obtain a yellow precipitate. The pellet was washed with deionized water three times, then redispersed with H_2O. $AgNO_3$ (170 mg, 1.0 mmol, 2 equiv.) was then added to the solution and stirred for 24 h at 40 °C in the dark. Then, the solution was filtered under reduced pressure to remove insoluble matter. Finally, NaN_3 (71.5 mg, 1.1 mmol, 2.20 equiv.) was added to the obtained clear liquid to continue the reaction for 24 h at 40 °C in the dark, and the light-yellow solid obtained was designated as **1** (yield 167 mg, 85%). Relevant analysis and characterization were performed using HPLC (Agilent 1260 Infinity III) and an Exactive Plus (Thermo Fisher) mass spectrometer.

Identification of binding sites of 1 on DNA

To identify putative binding sites of **1**, we performed MD ‘flooding’ simulations[31] on a structural model of 48mer DNA duplex (ATATA TATCG CGCGC GCCCC CCCCG GGGGG GGAAA AAAAA TTTTT TTT). We considered a system comprising one DNA duplex along with a large number of molecules of **1**, which were initially dispersed in the aqueous phase. During the MD simulations, position restraint with a weak force constant of 10 kJ (mol nm^2)$^{-1}$ was applied to the DNA duplex to ensure that the conformation of DNA was not significantly changed upon the loading of **1**. MD replicas (10) were performed, and these obtained trajectories were used to explore the possible binding modes of **1** on the DNA duplex.

To extract distinct configurations from our large dataset of molecular configurations, we analysed the equilibrated configurations of the system and focused on the regions close to the DNA base pairs that were characterized by high densities of **1**. We identified the binding sites of **1** on the DNA duplex using the following criteria: (1) **1** is located near DNA base pairs rather than the phosphate backbone; (2) the closest distance between **1** and the DNA molecule is <5 Å; and (3) the structure of **1** being integrated with the DNA duplex remains stable for >50 ns. The location distribution of **1** was calculated using the statistical algorithm below.

$$C(i) = \sum_{j=1}^{N_1} \sum_{k=1}^{N_2} S_j(t_k) \tag{1}$$

$$P(i) = C(i) / \sum_i C(i) \tag{2}$$

In the above formula, $t_k = kt_0/N_2$, t_0 is the total simulation time, N_2 is the sampling interval and was set to 10 herein, N_1 is the number of trajectory replicas, i represents the base-pair sequence types and $P(i)$ is the final distribution probability.

MD simulations

All MD simulations were performed with GROMACS2022 (ref. 39), and the produced trajectories were visualized using the VMD software package[40]. The DNA duplex (sequence: ATATA TATCG CGCGC GCCCC CCCCG GGGGG GGAAA AAAAA TTTTT TTT) was generated using the 'nab' programme in Ambertools22 (ref. 41). The DNA duplex was modelled using the all-atom AMBER99/bsc0 force field[42], while **1** was modelled using the generalized Amber force field (GAFF)[43]. The partial charges for each atom of **1** were calculated using DFT at the level of restricted Hartree–Fock with the 6-31G* basis set using Gaussian09 (ref. 44). The restricted electrostatic potential (RESP) technique was used to derive individual charges[45]. The bonded interactions of platinum-coordinated species were derived using the 'Para-freq' programme[46], which derives the bonded parameters from a single frequency calculation with the minimum energy state structure[47] (Extended Data Table 1). The TIP3P water molecules were used in our simulations.

The system was built with 1 DNA duplex, 300 molecules of **1**, solvated in a simulation box with 54,000 water molecules, with dimensions of ~99 Å×99 Å × 179 Å. Na^+ and Cl^- ions were added to neutralize the simulation system. The simulation timestep was set to 2 fs, and each simulation replica lasted 1 µs. A V-rescale thermostat (time constant 0.1 ps) was employed to maintain the temperature at 298.15 K, whereas the Berendsen isotropic algorithm (time constant 5.0 ps) regulated the pressure at 1 bar. Periodic boundary conditions were implemented, with long-range electrostatic interactions handled via the particle mesh Ewald method and Van der Waals interactions truncated at 1.0 nm. In addition, the LINCS algorithm was used to constrain hydrogen-involving bonds in both solvent and solute, and 10 independent simulation replicas were performed to deduce the binding distribution of complex **1** on the DNA duplex.

Electronic structure and reaction pathway calculations

The above MD simulations suggested that **1** locates at the GC step of the DNA duplex, with $-N_3$ groups connecting onto the $-NH_2$ groups of cytosine bases (see Fig. 1 for the structures). The two neighbouring GC base pairs together with the bounded **1** were adopted as the starting structure for electronic structure calculations. The geometry optimizations and Hessian matrix calculations for the two neighbouring GC base pairs coordinated with one molecule of **1** were performed with the Gaussian09 software package. The PBE0 hybrid density functional and def2-SVP basis set, and a quasi-relativistic 60-electron pseudopotential (ECP60MWB) together with D3 empirical dispersion corrections with Becke–Johnson damping, were used for platinum (that is, PBE0-D/def2-SVP for platinum). To save on computational power, PBE0-D/6-311G* was employed for other atoms of the studied system. The obtained geometries were used as the structural basis for subsequent energy, Gibbs free energy (at 298.15 K) calculations. Intrinsic reaction coordinate calculations were carried out to validate the transition states that link the anticipated reactants and corresponding products along the free-energy surface.

We calculated the reaction mechanism of platinonitrene compounds **2** (Fig. 1g,h, at singlet and triplet state) and **3** (Fig. 1i, at singlet and quintet state) with cytosine bases. The binding of platinonitrene **2** onto the GC step is relatively more stable at its singlet state by 11.8 kcal mol^{-1} in free energy than the triplet state. For platinonitrene **2**, N-N coupling can occur at the upper (Fig. 1g) or the lower (Fig. 1h) cytosine of the GC step. The N-N coupling products (**I2** and **I3'**) were found to be thermodynamically favoured than their triplet states (Fig. 1g,h). Complex **2** in path **h** (Fig. 1h) first achieved the proton transfer from amine to nitrene via HAA, resulting in the intermediate **I3**, followed by a downhill N-N coupling towards **I3'**. Despite the similar structures for **I2** and **I3'**, the difference in stereochemistry between them produces a substantial discrepancy in free energy. For platinonitrene **3** (Fig. 1i), the proton transfer from the amine group of the upper cytosine towards nitrene assists the N-N bonding between them (**I4**). **I4** experiences structural transformations to achieve HAA from the other coordinated cytosine (**I5**). The intramolecular N-N coupling of **I5** is a downhill process, which results in the final product **I5'**.

NLMO analysis

The spin density and NLMO analysis of metallonitrenes **2** and **3** was performed using the Multiwfn software (v.3.8dev)[48]. The isosurfaces of NLMOs were set at $0.05a_0^{-3/2}$ and the doubly occupied orbitals were calculated by averaging the α and β spin orbitals. The isosurfaces were visualized using the VMD software package.

In vitro assessment

To detect the effect of **1** on apoptosis, mitochondrial membrane potential, superoxide anion production and ATP production in cell culture medium, CT26 cells were cultured at the same concentration in culture flasks and treated with 2 µg ml^{-1} or 20 Gy X-ray[24,49] through the iSMAART[50] equipment or SHARP 1000 (Raycision Medical Technology), which is an integrated small-animal investigation system with high-quality quantitative optical tomography. After 24 h, the cells or the culture supernatants were treated according to vendor protocols and detected using a microplate reader (SpectraMax iD3) or flow cytometer (CytoFLEX Flow Cytometer, Beckman).

To detect DNA damage at the single-cell level, a comet assay was performed using the DNA Damage Comet Assay kit (Beyotime, C2041S). Briefly, CT26 cells were cultured at the same concentration in culture flasks and treated with 2 µg ml^{-1} **1** or 20 Gy X-ray overnight. Then, cells were collected and cell density was adjusted to 1×10^6 ml^{-1} using PBS. The cell suspension was mixed with a low melting point agarose gel at 37 °C and placed on a glass slide pre-coated with a normal melting point agarose gel. Cell lysis and DNA unwinding under alkaline conditions were then performed, and horizontal electrophoresis was performed at a low voltage of 25 V. Finally, the glass slides were stained using propidium iodide solution and images were captured using a confocal laser scanning microscope (Leica STELLARIS 8 STED). Cell DNA damage was analysed via CASP 1.2.3b1. According to the percentage of DNA in the tail of the cell (that is, tail DNA%), DNA damage of the cells was classified into 5 levels: 0–6% was level 0, 6.1–17.0% was level 1, 17.1–35% was level 2, 35.1–60% was level 3 and 60.1–100% was level 4.

For the clonogenic assay, CT26 cells were uniformly cultured in flasks, treated with 2 µg ml^{-1} **1** or varying X-ray doses, then seeded at 500 cells per 10 cm dish and cultured for 12 days. Colonies were fixed with 6.0% (v/v) glutaraldehyde, stained with 0.5% (w/v) crystal violet and counted.

Antitumour efficacy of 1-sensitized RT in the CT26 tumour model

For the study of antitumour efficacy, BALB/c mice (female, 6–8 weeks) were subcutaneously injected with 5×10^5 CT26 cells into the right flank on day 0. All mice were randomly divided into the following four groups before drug administration: control, RT, **1** and **1** + RT. Tumour volume was calculated according to the formula: $V = 0.5 \times \text{length} \times \text{width}^2$. Tumour volume was measured and recorded every 2 or 3 days, and when the tumour volume reached ~0.1 cm^3, mice were treated according to grouping. Complex **1** (5 mg kg^{-1}) was injected intratumourally, followed by radiation therapy (3 Gy) to the tumour areas 6 h later every other day, for a total of three times. When the tumour volume reached 3 cm^3, the mice were euthanized.

Antitumour efficacy of 1-sensitized RT in the orthotopic glioblastoma model

For the study of antitumour efficacy, 5×10^4 GL261-luc cells were inoculated intracranially at 2.5 mm anterior, 2.5 mm to the right side of the bregma and 3.5 mm deep into the brain of C57BL/6J mice (female, 6–8 weeks) on day 0. All mice were randomly divided into the following four groups before drug administration: Blank, RT, **1** and **1** + RT. The bioluminescence signal from the GL261-luc brain tumours was observed using the IVIS imaging system (Perkin Elmer) after the injection of 150 mg kg^{-1} luciferin. Complex **1** (5 mg kg^{-1}) was injected intravenously (i.v.), followed by radiotherapy (3 Gy) to the brain tumour areas 6 h later on days 7, 9 and 11. IVIS imaging was performed every 4 or 5 days. When weight loss was more than 20%, the mice were euthanized.

Flow cytometric analysis of tumour-infiltrating T cell subsets

After all dosing was complete, tumour tissues of all mice were collected. Then, collected tumour tissues were mechanically minced with a GentleMACS Dissociator (Miltenyi Biotec) and digested with collagenase IV, hyaluronidase and DNase at 37 °C for 30 min to obtain single-cell suspensions. After treatment with red blood cell lysis buffer on ice for 10 min, the acquired single cells were incubated with low-affinity blocking reagent for 10 min on ice before staining in Hanks' balanced salt solution containing 0.5% FBS with flow cytometry antibodies in accordance with manufacturer instructions. Briefly, the dead cell staining kit was first used to distinguish live from dead cells. Then, all samples were blocked with CD16/CD32 antibodies to reduce non-specific staining on ice, followed by surface staining using anti-mouse CD45-eFluor 450, anti-mouse CD3-APC-eFluor 780, anti-mouse CD4-Alexa Fluor 488 and anti-mouse CD8α-APC. Finally, all samples were fixed and permeabilized, and anti-mouse Foxp3-PE-eFluor 610 was used to stain intracellular antigen. All samples were stored at 4 °C and analysed using a CytoFLEX flow cytometer as soon as possible within 24 h. Similarly, anti-mouse IFNγ-APC, anti-mouse CD107a-Brilliant Violet 421, anti-mouse TIM3-APC and anti-mouse PD1-APC were used to further stain CD8^{+} T cells, and anti-mouse CD39-PE/Cy7, anti-mouse CD44-Alexa Fluor 700, anti-mouse CD69-Brilliant Violet 605, anti-mouse Nrp-1-Brilliant Violet 421, anti-mouse Helios-PE/Cy7, anti-mouse GITR-APC and anti-mouse ICOS- Alexa Fluor 700 were used to further stain Treg cells. All gating strategies are provided in Supplementary Figs. 39–41.

Flow cytometric analysis of maturation of DCs in TDLNs

After all dosing was complete, TDLNs of all animals were collected and treated as described earlier to prepare single-cell suspensions. Anti-mouse CD11c-PE-Cy7, anti-mouse CD80-BV421 and anti-mouse CD86-APC were used to stain surface antigens. Then, all samples were analysed using the CytoFLEX flow cytometer as soon as possible within 24 h. Gating strategies are provided in Supplementary Fig. 39.

Differentiation induction of Treg cells

Briefly, 96-well plates were first pre-coated with 2 μg ml^{-1} anti-CD3 at 4 °C overnight. Then, spleens were collected from C57BL/6-Foxp3$^{\mathrm{tm1Flv}}$/J mice and CD4 T cells were sorted via magnetic beads using MojoSort Mouse CD4 Naïve T Cell Isolation kits. The sorted CD4 T cells were resuspended in RPMI 1640 medium, then seeded into pre-coated 96-well plates at a density of 100,000 cells per well. Anti-CD28, IL-2 and TGF-β were added into wells to reach the concentration of 1 μg ml^{-1}, 100 IU ml^{-1} and 5 ng ml^{-1}, respectively. Complex **1** was added to the wells at different concentrations, incubated with the cells, and cells cultured with a constant 5% CO_2 at 37 °C for 48 h. Finally, flow cytometry was used to detect the differentiation efficiency and apoptosis of each cell subset.

CFSE staining to assay the proliferation of each T cell subset

Briefly, 96-well plates were first pre-coated with 1 μg ml^{-1} anti-CD3 and anti-CD28 at 4 °C overnight. Spleens were collected from C57BL/6-Foxp3$^{\mathrm{tm1Flv}}$/J mice, then ground to obtain single-cell suspensions. After treatment with red blood cell lysis buffer, cells were resuspended and counted, then stained with CFSE in medium. After washing off excess CFSE staining solution, cells were resuspended in RPMI 1640 medium, then seeded into pre-coated 96-well plates at a density of 500,000 cells per well. Complex **1** was then added to the wells at different concentrations, incubated with the cells, and cells cultured with a constant 5% CO_2 at 37 °C. Finally, flow cytometry was used to detect the proliferation of each T cell subset.

Immunofluorescence of tumour tissues

After all dosing was complete, tumour tissues of all mice were collected and fixed in paraformaldehyde solution for 48 h at room temperature. Tumour tissues were first embedded and sectioned, followed by blocking. HMGB1 and CRT in tumour tissues were labelled with fluorescein FITC and Cy3, respectively, by sequential incubation with primary and secondary antibodies. Ki67 (FITC), caspase-3 (Cy3) and γH2AX (FITC) in tumour tissues were also labelled using the same method. Images of all slices were captured using a confocal laser scanning microscope (Zeiss 710 and Leica STELLARIS 8 STED).

RNA-seq analysis of tumour tissues

After all dosing was complete, tumour tissues of all mice were collected and washed with PBS buffer three times. The tumour samples were then subjected to RNA extraction and RNA quality testing, immediately followed by library construction, library purification, library detection and library quantification. Next, Ultra RNA Library Prep kit for Illumina (NEB, E7530) was used for RNA library preparation. After the library was constructed, a Qubit 2.0 fluorometer was used for preliminary quantification. Hisat2 (v.2.2.1) was used to construct the genome indexes and Hisat2 (v.2.2.1) was used to calculate the read counts of each gene. Finally, the sequencing cluster was generated and sequenced on the machine. Bioinformatics analysis, mainly differential gene analysis including cluster analysis, Gene Ontology (GO) enrichment analysis and Kyoto Encyclopedia of Genes and Genomes (KEGG) enrichment analysis, was performed on the original sequencing data. Raw sequencing reads were aligned to the Ensembl Release mm39 reference genome using STAR (v.2.5.3a) with default parameters. Following alignment, HTSeq (v.2.0.1) was employed to quantify read counts for each gene. DESeq2 was utilized for differential expression analysis. Pairwise comparisons were conducted among the four groups: Blank, RT, **1**, and **1** + RT. Genes were considered significantly differentially expressed if the adjusted *P* value (P_{adj}) was <0.05 and the fold change was >2. GO analysis was performed using the Metascape platform. Genes within each hierarchical clustering group were analysed to identify significantly enriched GO terms. The analysis encompassed categories of biological processes, molecular functions and cellular components to comprehensively understand the functional importance of differentially expressed genes within each clustering group.

Immunotherapeutic studies of 1-sensitized low-dose RT in combination with αPD-1

For the study on improving immunotherapy, BALB/c mice (female, 6–8 weeks) were subcutaneously injected with 5 × 10^{5} CT26 cells into the right flank on day 0. All mice were randomly divided into the following five groups before drug administration: Blank, αPD-1, RT + αPD-1, **1** + RT, and **1** + RT + αPD-1. On days 11, 13 and 15, **1** (5 mg kg^{-1}) was injected intratumourally, followed by a lower dose of radiation therapy (1 Gy) to the tumour areas 6 h later. αPD-1 (5 mg kg^{-1}) was injected intraperitoneally on days 13, 16 and 19. When the tumour volume reached 3 cm^{3}, the mice were euthanized.

Abscopal effect of 1-sensitized low-dose RT in combination with αPD-1

For the study on the abscopal effect, mice were subcutaneously injected with 5 × 10^{5} CT26 cells into the right flank (primary tumour) on day 0 and then injected with 5 × 10^{5} CT26 cells into the left flank (secondary tumour) on day 4. All mice were randomly divided into the following three groups before drug administration: control, RT + αPD-1, and

1 + RT + αPD-1. On days 11, 13 and 15, **1** (5 mg kg^{-1}) was injected intratumourally to the primary tumour, followed by a lower dose of radiation therapy (1 Gy) to the primary tumour areas 6 h later. All treatments were directed only at the primary tumour. αPD-1 (5 mg kg^{-1}) was injected intraperitoneally on days 11, 14 and 17. The volumes of primary and secondary tumours were measured and recorded every 2 or 3 days. When the tumour volume reached 1.5 cm (ref. 3), the mice were euthanized.

On day 18, both primary and secondary tumours were collected and stained with anti-mouse CD45-eFluor 450, anti-mouse CD3-APC-eFluor 780, anti-mouse CD4-Alexa Fluor 488, anti-mouse CD8α-APC and anti-mouse Foxp3-PE-eFluor 610. TDLNs near the primary tumour were also collected and stained with anti-mouse CD11c-PE-Cy7, anti-mouse CD80-BV421 and anti-mouse CD86-APC. Then, all samples were analysed using the CytoFLEX flow cytometer as soon as possible within 24 h.

In vivo safety studies of 1

For the study on biosecurity, mice were subcutaneously injected with 5×10^5 CT26 cells into the right flank on day 0. All mice were randomly divided into the following six groups before drug administration: control, RT, oxaliplatin, oxaliplatin + RT, **1**, and **1** + RT. On days 11, 13 and 15, **1** (5 mg kg^{-1}) or oxaliplatin (5 mg kg^{-1}) was injected intravenously, followed by radiation therapy (3 Gy) to the tumour areas 6 h later. When the tumour volume reached 3 cm^3, the mice were euthanized.

After all dosing was complete, the sera of all mice were collected and used for biochemical analysis of liver and kidney markers. Heart, liver, spleen, lung and kidneys of mice were collected separately and then analysed by pathological section. Pt content (total amount of Pt in different tissues or organs, μg) and Pt concentration (the ratio of the total amount of Pt in different tissues or organs to the mass of that tissue or organ, ppm) after i.v. and i.t. were quantified via inductively coupled plasma–mass spectrometry (ICP–MS, Thermo Scientific, iCAP RQ).

Assessment of immune memory effects

For the analysis of immune memory effects, peripheral blood of treated mice was collected and compared to that of naive mice after the former mice were cured for 8 months. All samples were stained using CD3-APC-eFluor 780, anti-mouse CD8α-APC, anti-mouse CD44-FITC and anti-mouse CD62L-eFluor 450, and memory T cells were analysed using flow cytometry. All cured mice were rechallenged with 5×10^5 CT26 cells to assess whether the cured mice could resist tumour growth again.

Statistical analysis

No statistical methods were used to predetermine sample sizes, but our sample sizes are similar to those reported in previous publications[33]. All statistical analyses were performed with GraphPad Prism 8 and all values are presented as mean ± s.d. as indicated in figure captions. Replicates are independent biological samples. All flow cytometric analyses were carried out using a CytoFLEX flow cytometer (Beckman) and analysed with CytExpert v.2.3 and FlowJo v.10.6, and all gating strategies are provided in Supplementary Figs. 39–42. The sample sizes for in vitro, ex vivo and in vivo studies were based on previous published papers[6,27,33]. Mice for treatment groups were randomized, in which the groups were single blinded. The data analyses (including immunohistochemistry) were also single blinded. RNA-seq data were analysed single blinded. All in vitro studies were not blinded, as our experiments were not based on subjective measurements. No collected data were excluded from our analysis. One-way or two-way analysis of variance (ANOVA) was used for multiple comparisons when more than two groups were compared, and the Mann–Whitney test was used for two-group comparisons. The Kaplan–Meier method was used to perform survival difference analysis, and the log-rank test was used to determine the overall *P* value.

Reporting summary

Further information on research design is available in the Nature Portfolio Reporting Summary linked to this article.

Data availability

All relevant data supporting the results in this study are available within the paper. The raw and analysed datasets generated during the study are available for academic purposes from the corresponding authors upon request. RNA sequencing data that support the findings of this study are deposited and made publicly available in the NCBI Gene Expression Omnibus repository under accession number GSE314315. Source data are provided with this paper.

References

1. Petroni, G., Cantley, L. C., Santambrogio, L., Formenti, S. C. & Galluzzi, L. Radiotherapy as a tool to elicit clinically actionable signalling pathways in cancer. *Nat. Rev. Clin. Oncol.* **19**, 114–131 (2022).
2. Chabanon, R. M. et al. Targeting the DNA damage response in immuno-oncology: developments and opportunities. *Nat. Rev. Cancer* **21**, 701–717 (2021).
3. Schaue, D. & McBride, W. H. Opportunities and challenges of radiotherapy for treating cancer. *Nat. Rev. Clin. Oncol.* **12**, 527–540 (2015).
4. Weichselbaum, R. R., Liang, H., Deng, L. & Fu, Y.-X. Radiotherapy and immunotherapy: a beneficial liaison? *Nat. Rev. Clin. Oncol.* **14**, 365–379 (2017).
5. Keener, A. B. Making radiation oncology more personal. *Nature* **585**, S10 (2020).
6. Nishiga, Y. et al. Radiotherapy in combination with CD47 blockade elicits a macrophage-mediated abscopal effect. *Nat. Cancer* **3**, 1351–1366 (2022).
7. Ngwa, W. et al. Using immunotherapy to boost the abscopal effect. *Nat. Rev. Cancer* **18**, 313–322 (2018).
8. Grassberger, C., Ellsworth, S. G., Wilks, M. Q., Keane, F. K. & Loeffler, J. S. Assessing the interactions between radiotherapy and antitumour immunity. *Nat. Rev. Clin. Oncol.* **16**, 729–745 (2019).
9. Hiniker, S. M. & C. D., Knox SJ. Abscopal effect in a patient with melanoma. *N. Engl. J. Med.* **366**, 2035–2036 (2012).
10. De Ruysscher, D. et al. Radiotherapy toxicity. *Nat. Rev. Dis. Primers* **5**, 13 (2019).
11. Price, J. M., Prabhakaran, A. & West, C. M. L. Predicting tumour radiosensitivity to deliver precision radiotherapy. *Nat. Rev. Clin. Oncol.* **20**, 83–98 (2023).
12. Wang, H., Mu, X., He, H. & Zhang, X.-D. Cancer radiosensitizers. *Trends Pharmacol. Sci.* **39**, 24–48 (2018).
13. Gill, M. R. & Vallis, K. A. Transition metal compounds as cancer radiosensitizers. *Chem. Soc. Rev.* **48**, 540–557 (2019).
14. Sun, J. et al. A platinum(II) metallonitrene with a triplet ground state. *Nat. Chem.* **12**, 1054–1059 (2020).
15. Domenianni, L. I. et al. Photoinduced metallonitrene formation by N_2 elimination from azide diradical ligands. *Angew. Chem. Int. Ed.* **62**, e202309618 (2023).
16. Wentrup, C. Carbenes and nitrenes: recent developments in fundamental chemistry. *Angew. Chem. Int. Ed.* **57**, 11508–11521 (2018).
17. Vreeken, V. et al. C–H activation of benzene by a photoactivated NiII(azide): formation of a transient nickel nitrido complex. *Angew. Chem. Int. Ed.* **54**, 7055–7059 (2015).
18. Henning, H., Hofbauer, K., Handke, K. & Stich, R. Unusual reaction pathways in the photolysis of diazido(phosphane)nickel(II) complexes: nitrenes as intermediates in the formation of nickel(0) complexes. *Angew. Chem. Int. Ed.* **36**, 408–410 (1997).

19. Carsch, K. M. et al. Synthesis of a copper-supported triplet nitrene complex pertinent to copper-catalyzed amination. *Science* **365**, 1138–1143 (2019).
20. Jung, H. et al. Mechanistic snapshots of rhodium-catalyzed acylnitrene transfer reactions. *Science* **381**, 525–532 (2023).
21. Baek, Y. et al. C–H amination mediated by cobalt organoazide adducts and the corresponding cobalt nitrenoid intermediates. *J. Am. Chem. Soc.* **142**, 11232–11243 (2020).
22. Wang, H. et al. Nitrene-mediated intermolecular N–N coupling for efficient synthesis of hydrazides. *Nat. Chem.* **13**, 378–385 (2021).
23. Thornton, A. R., Martin, V. I. & Blakey, S. B. Pi-nucleophile traps for metallonitrene/alkyne cascade reactions: a versatile process for the synthesis of α-aminocyclopropanes and β-aminostyrenes. *J. Am. Chem. Soc.* **131**, 2434–2435 (2009).
24. Geng, J. et al. Switching on prodrugs using radiotherapy. *Nat. Chem.* **13**, 805–810 (2021).
25. Guillemard, L., Kaplaneris, N., Ackermann, L. & Johansson, M. J. Late-stage C–H functionalization offers new opportunities in drug discovery. *Nat. Rev. Chem.* **5**, 522–545 (2021).
26. Cosio, M. N. & Powers, D. C. Prospects and challenges for nitrogen-atom transfer catalysis. *Nat. Rev. Chem.* **7**, 424–438 (2023).
27. Herrera, F. G. et al. Low-dose radiotherapy reverses tumor immune desertification and resistance to immunotherapy. *Cancer Discov.* **12**, 108–133 (2022).
28. Scott, J. G. et al. A genome-based model for adjusting radiotherapy dose (GARD): a retrospective, cohort-based study. *Lancet Oncol.* **18**, 202–211 (2017).
29. Cheung, E. C. & Vousden, K. H. The role of ROS in tumour development and progression. *Nat. Rev. Cancer* **22**, 280–297 (2022).
30. Kornepati, A. V. R., Rogers, C. M., Sung, P. & Curiel, T. J. The complementarity of DDR, nucleic acids and anti-tumour immunity. *Nature* **619**, 475–486 (2023).
31. Vemparala, S., Domene, C. & Klein, M. L. Interaction of anesthetics with open and closed conformations of a potassium channel studied via molecular dynamics and normal mode analysis. *Biophys. J.* **94**, 4260–4269 (2008).
32. Parikh, A. R. et al. Radiation therapy enhances immunotherapy response in microsatellite stable colorectal and pancreatic adenocarcinoma in a phase II trial. *Nat. Cancer* **2**, 1124–1135 (2021).
33. Min, Y. et al. Antigen-capturing nanoparticles improve the abscopal effect and cancer immunotherapy. *Nat. Nanotechnol.* **12**, 877–882 (2017).
34. Hoff, P. M. Oxaliplatin-related neurotoxicity: is chelation the solution? *Nat. Clin. Pract. Oncol.* **1**, 78–79 (2004).
35. Argyriou, A. A., Bruna, J., Genazzani, A. A. & Cavaletti, G. Chemotherapy-induced peripheral neurotoxicity: management informed by pharmacogenetics. *Nat. Rev. Neurol.* **13**, 492–504 (2017).
36. Kim, H. P. et al. The clinical spectrum and diagnosis of oxaliplatin liver injury in the era of nonalcoholic fatty liver disease. *Clin. Gastroenterol. Hepatol.* **19**, 2199–2201 (2021).
37. Wilson, W. R. & Hay, M. P. Targeting hypoxia in cancer therapy. *Nat. Rev. Cancer* **11**, 393–410 (2011).
38. Singleton, D. C., Macann, A. & Wilson, W. R. Therapeutic targeting of the hypoxic tumour microenvironment. *Nat. Rev. Clin. Oncol.* **18**, 751–772 (2021).
39. Van Der Spoel, D. et al. GROMACS: fast, flexible, and free. *J. Comput. Chem.* **26**, 1701–1718 (2005).
40. Humphrey, W., Dalke, A. & Schulten, K. V. M. D. Visual molecular dynamics. *J. Mol. Graph.* **14**, 33–38 (1996).
41. Salomon-Ferrer, R., Case, D. A. & Walker, R. C. An overview of the Amber biomolecular simulation package. *WIREs Comput. Mol. Sci.* **3**, 198–210 (2013).
42. Pérez, A. et al. Refinement of the AMBER force field for nucleic acids: improving the description of α/γ conformers. *Biophys. J.* **92**, 3817–3829 (2007).
43. Wang, J., Wolf, R. M., Caldwell, J. W., Kollman, P. A. & Case, D. A. Development and testing of a general amber force field. *J. Comput. Chem.* **25**, 1157–1174 (2004).
44. Frisch, M. J. et al. Gaussian 09, Revision D.01 (Gaussian, Inc., 2009).
45. Bayly, C. I., Cieplak, P., Cornell, W. & Kollman, P. A. A well-behaved electrostatic potential based method using charge restraints for deriving atomic charges: the RESP model. *J. Phys. Chem.* **97**, 10269–10280 (1993).
46. Burger, S. K. et al. Automated parametrization of AMBER force field terms from vibrational analysis with a focus on functionalizing dinuclear zinc(II) scaffolds. *J. Chem. Theory Comput.* **8**, 554–562 (2012).
47. Pereira, A. F., Prandi, I. G. & Ramalho, T. C. Parameterization and validation of a new force field for Pt(II) complexes of 2-(4′-amino-2′-hydroxyphenyl)benzothiazole. *Int. J. Quantum Chem.* **121**, e26525 (2021).
48. Lu, T. & Chen, F. Multiwfn: a multifunctional wavefunction analyzer. *J. Comput. Chem.* **33**, 580–592 (2012).
49. Ding, Z. et al. Radiotherapy reduces N-oxides for prodrug activation in tumors. *J. Am. Chem. Soc.* **144**, 9458–9464 (2022).
50. Chen, J. et al. Accurate and early metastases diagnosis in live animals with multimodal X-ray and optical imaging. *Int. J. Radiat. Oncol. Biol. Phys.* **115**, 511–517 (2023).

Acknowledgements

This work was supported by: the National Natural Science Foundation of China (32271433, 32471437 and 31971299); 2025IHM01180, Start-Up grants KY2060000124 and KJ2060190030 from the University of Science and Technology of China and Fundamental Research Funds for the Central Universities (YD9100002031, WK2060190101) to Y.M. ; the National Natural Science Foundation of China (22422306) and National Key R&D Program of China (2024YFA1509203) to S.X.; the Natural Science Foundation of Anhui Province (2208085J48) and Hefei Comprehensive National Science Center Institute of Health and Medicine Project (DJK-LX-2022006, 2023IHM01044) to B.L.; the National Key R&D Program of China (2022YFA1303200) to K.Q, and the National Natural Science Foundation of China grants (T2125012 and 92574202) and Strategic Priority Research Program of Chinese Academy of Sciences (XDB0940301) to K.Q.; funding from the Global STEM Professorship, start-up fund (Grant No. 2023-Xing, HKPU), and Projects of RISA PolyU (UGC) (1-CDN9) to B.X. The work described in this paper was also partially supported by a grant from the NSFC/RGC Joint Research Scheme sponsored by the Research Grants Council of Hong Kong and the National Natural Science Foundation of China (Project No. N_PolyU521/25) to B.X.; and by the Fundamental Research Funds for the Central Universities (WK2060000099) to Y.X. The funders had no role in study design, data collection and analysis, decision to publish or preparation of the manuscript.

Author contributions

Y.M. conceived and designed the experiments with G.C. G.C. and X.L. performed the efficacy study. G.C. also performed the mechanistic study. Y. Huang and S.X. performed the calculations. C.Z., G.C., C.G. and H.Z. conducted radiotherapy for in vitro and in vivo experiments. G.C., H.F., Q. Zhang and B.L. designed and performed the flow cytometry analysis of Treg cells. G.C., K.L. and K.Q. performed the analysis of RNA sequencing. K.W., Qilong Zhu, R.D. and Y. He helped to perform the experiments at cellular level. Qiuhong Zhu and W.Z. helped to establish the glioblastoma model. G.C. and Y.M. wrote the manuscript. All authors analysed and discussed the data, revised the manuscript, and approved the submission.

Competing interests

The authors declare no competing interests.

Additional information

Extended data is available for this paper at https://doi.org/10.1038/s41551-026-01612-y.

Supplementary information The online version contains supplementary material available at https://doi.org/10.1038/s41551-026-01612-y.

Correspondence and requests for materials should be addressed to Kun Qu, Bofeng Li, Shiyan Xiao or Yuanzeng Min.

Peer review information *Nature Biomedical Engineering* thanks the anonymous reviewers for their contribution to the peer review of this work. Peer reviewer reports are available.

---

[1]Department of Endocrinology and Metabolism, Institute of Endocrine and Metabolic Diseases, The First Affiliated Hospital of USTC, Division of Life Sciences and Medicine; Hefei National Research Center for Physical Sciences at the Microscale; Department of Chemistry, University of Science and Technology of China, Hefei, Anhui, P. R. China. [2]Key Laboratory of Precision and Intelligent Chemistry, University of Science and Technology of China, Hefei, Anhui, P. R. China. [3]School of Physical Sciences and Ion Medical Research Institute, University of Science and Technology of China, Hefei, Anhui, P. R. China. [4]Department of Medical Oncology, The First Affiliated Hospital of USTC, Division of Life Sciences and Medicine, University of Science and Technology of China, Hefei, Anhui, P. R. China. [5]Division of Life Sciences and Medicine, University of Science and Technology of China, Hefei, Anhui, P. R. China. [6]Intelligent Pathology Institute, The First Affiliated Hospital of USTC, Division of Life Sciences and Medicine, University of Science and Technology of China, Hefei, Anhui, P. R. China. [7]Biomedical Research Imaging Center, Department of Radiology, and UNC Lineberger Comprehensive Cancer Center, University of North Carolina-Chapel Hill, Chapel Hill, NC, USA. [8]Department of Microbiology and Immunology, University of North Carolina at Chapel Hill, Chapel Hill, NC, USA. [9]School of Chemistry, Chemical Engineering and Biotechnology, Nanyang Technological University, Singapore, Singapore. [10]Department of Applied Biology and Chemical Technology, The Hong Kong Polytechnic University, Kowloon, Hong Kong SAR, China. [11]Departments of Diagnostic Radiology, Surgery, Chemical and Biomolecular Engineering, and Biomedical Engineering, Yong Loo Lin School of Medicine and College of Design and Engineering, National University of Singapore, Singapore, Singapore. [12]Clinical Imaging Research Centre, Centre for Translational Medicine, Yong Loo Lin School of Medicine, National University of Singapore, Singapore, Singapore. [13]Nanomedicine Translational Research Program, Yong Loo Lin School of Medicine, National University of Singapore, Singapore, Singapore. [14]Institute of Molecular and Cell Biology, Agency for Science, Technology, and Research (A*STAR), Proteos, Singapore, Singapore. [15]Department of Radiation Oncology, Simmons Comprehensive Cancer Center, UT Southwestern Medical Center, Dallas, TX, USA. [16]School of Chemistry and Materials Science, Experimental Center of Engineering and Material Sciences, School of Engineering Science, University of Science and Technology of China, Hefei, Anhui, P. R. China. ✉e-mail: qukun@ustc.edu.cn; libf@ustc.edu.cn; xiaosy@ustc.edu.cn; minyz@ustc.edu.cn

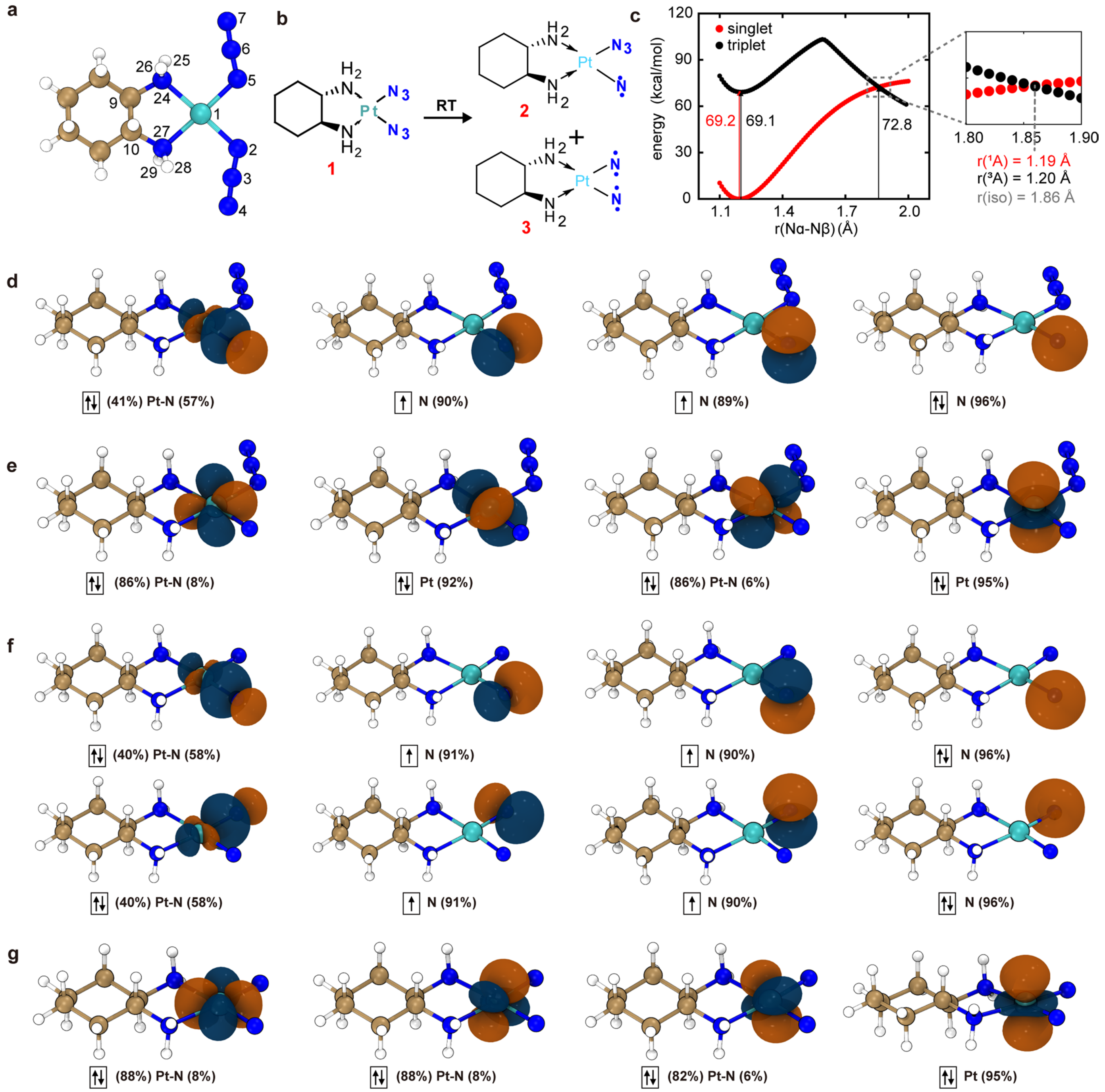

Extended Data Fig. 1 | Characteristic NLMOs resulting from NBO analysis support the platinonitrene description of complex 2 and 3. a, Structural representation of 1. **b**, N2 releases from 1 under X-ray irradiation, and produces metallonitrene compound 2 and 3. **c**, Scan of the Nα-Nβ bond length for singlet and triplet states of 1 to illustrate the interplay of singlet and triplet states during the loss of N2 from the molecule of 1. The triplet state of complex 2 is strongly stabilized by 12.7 kcal/mol compared with its singlet state. The calculations were performed at the level of PBE0-D/def2-TZVPP, and the step size during the scan is set to 0.01 Å. **d-g**, Characteristic NLMOs resulting from an NBO analysis. **d-e**, Pt-N σ-bond, singly occupied py, pz orbitals and s-type lone pair localized at N atom (**d**), and Pt-centred and doubly occupied d orbitals (**e**) of 2, which has only one nitrene group. f-g, Pt-N σ-bond, singly occupied py, pz orbitals and s-type lone pair localized at N atom (**f**), and Pt-centred and doubly occupied d orbitals (**g**) of 3, which has two nitrene groups. d to g show that the covalent Pt-N σ-bonds polarized towards nitrogen, a s-type lone pair and two singly occupied p-type NLMOs on the nitrene N atom as well as four essentially nonbonding Pt d orbitals which shared only insignificant N contributions (Pt-N Mayer bond order: 1.15 for 2 and 1.06 for 3).

https://doi.org/10.1038/s41551-026-01612-y

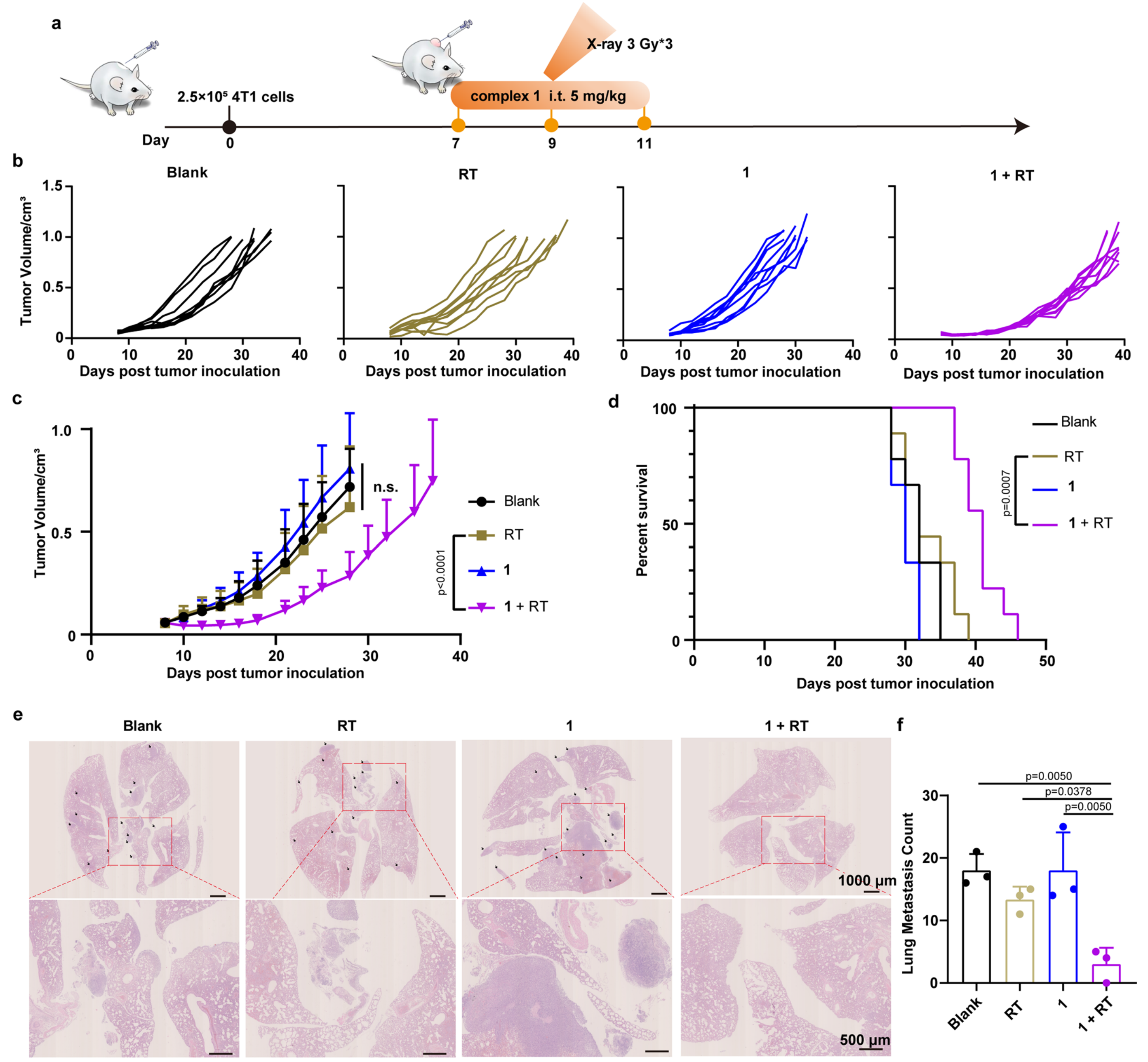

Extended Data Fig. 2 | Complex 1 sensitized RT effectively inhibits the growth and metastasis of 4T1 tumours. a, Schemes of 4T1 tumour inoculation and therapies. **b**, Tumour growth curves of each mouse. **c**, Average tumour growth curves showed 1 sensitized RT effectively inhibited the growth of 4T1 tumours (n = 9). Tumour growth with the passage of time was compared by two-way ANOVA (Tukey's test). **d**, Survival curves showed 1 sensitized RT prolonged the survival time of mice (n = 9). Differences in survival were determined for each group by the Kaplan-Meier method, and the overall P value was calculated by the log-rank test. **e**, Representative lung pathology sections of mice showed that 1 sensitized RT effectively inhibited lung metastasis of 4T1 tumours. Black arrow, pulmonary nodules. **f**, Lung metastasis count of mice (n = 3). One-way ANOVA multiple comparisons (Tukey's multiple comparisons test) were used when more than two groups were compared. All the values in the present study are presented as the mean ± s.d., and all replicates are biological independent samples.

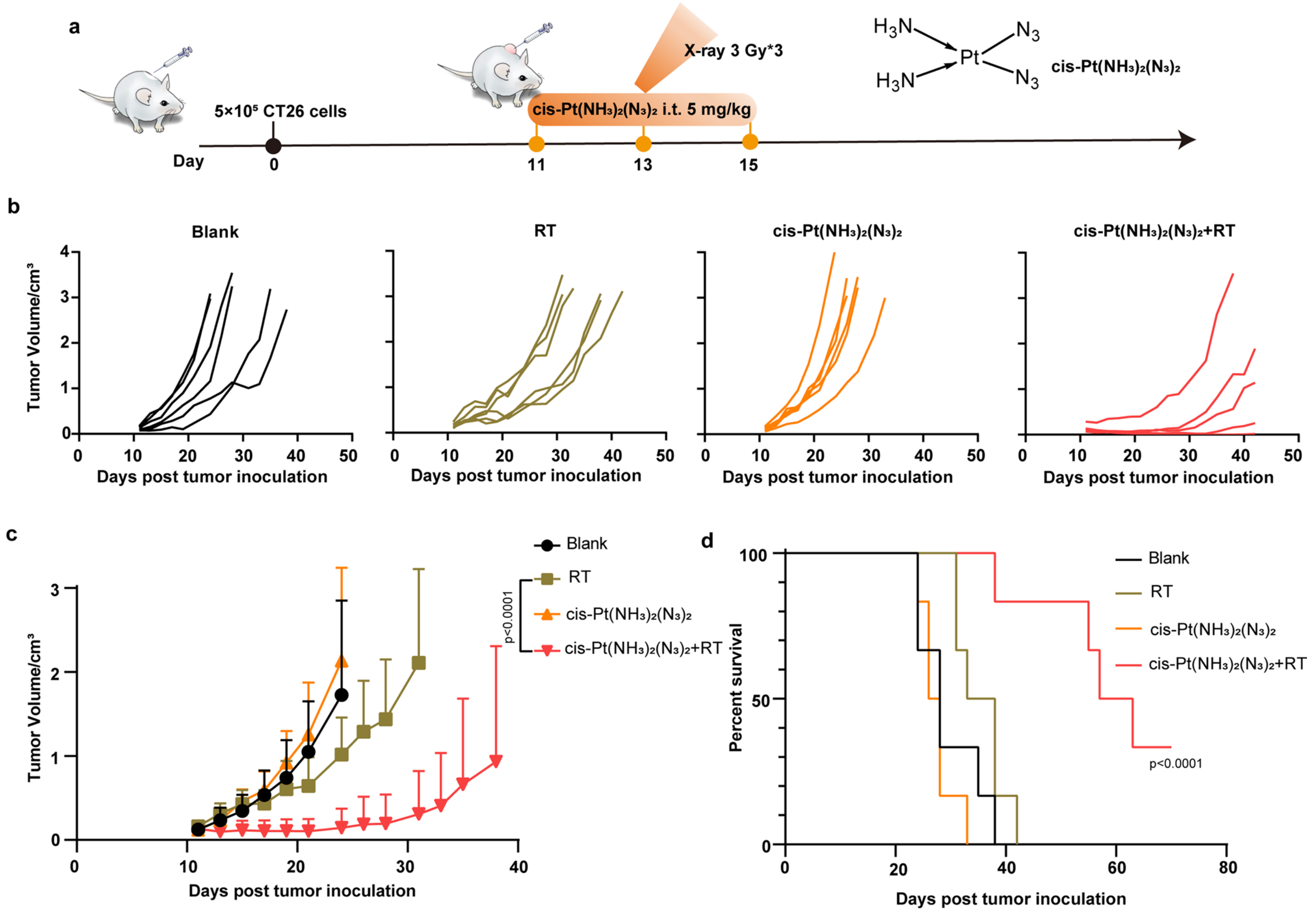

Extended Data Fig. 3 | cis-Pt(NH3)2(N3)2 sensitized RT effectively inhibits the growth of established CT26 tumours. a, Schemes of CT26 tumour inoculation and therapies. **b**, Tumour growth curves of each mouse. **c**, Average tumour growth curves showed cis-Pt(NH3)2(N3)2 sensitized RT effectively inhibited the growth of established CT26 tumours (n = 6). Tumour growth with the passage of time was compared by two-way ANOVA (Tukey's test). **d**, Survival curves showed cis-Pt(NH3)2(N3)2 sensitized RT prolonged the survival time of mice (n = 6). Differences in survival were determined for each group by the Kaplan–Meier method, and the overall P value was calculated by the log-rank test. All the values in the present study are presented as the mean ± s.d., and all replicates are biological independent samples.

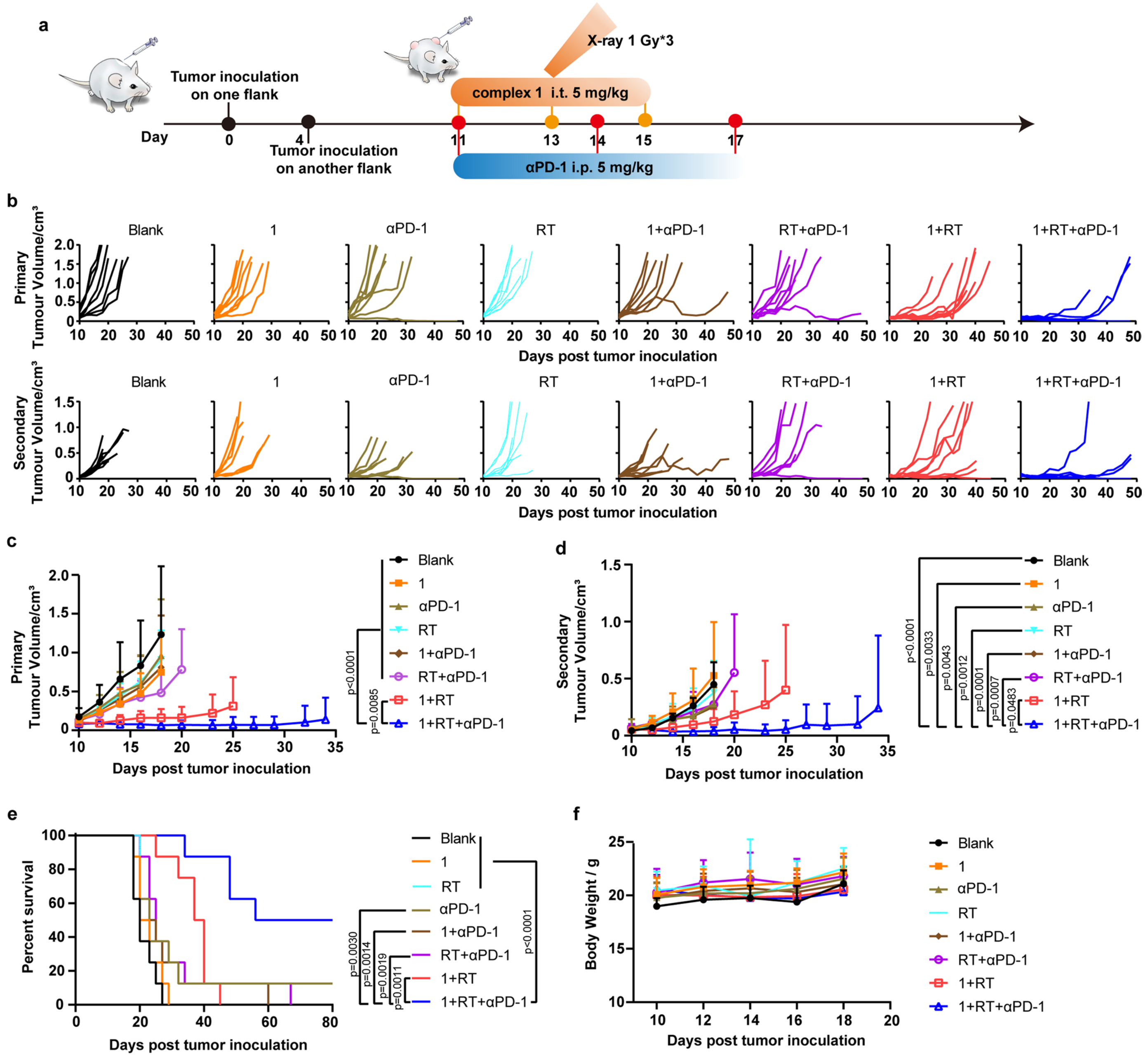

Extended Data Fig. 4 | Complex 1 sensitized RT enhances abscopal effect on syngeneic CT26 tumour model. **a**, Schemes of primary and secondary tumour inoculation and therapies. **b**, Primary and secondary tumour growth curves of each mouse showed 1 in combination with RT and αPD-1 suppress growth of bilateral tumours. **c**, Average primary tumour growth curves of each group (n = 8). **d**, Average secondary tumour growth curves of each group (n = 8). Tumour growth with the passage of time was compared by two-way ANOVA (Tukey's test). **e**, Survival curves showed 1 in combination with RT and αPD-1 prolonged survival time of mice in bilateral tumour model (n = 8). Differences in survival were determined for each group by the Kaplan–Meier method, and the overall P value was calculated by the log-rank test. **f**, Body weight change curve of mice (n = 8). All the values in the present study are presented as the mean ± s.d., and all replicates are biological independent samples.

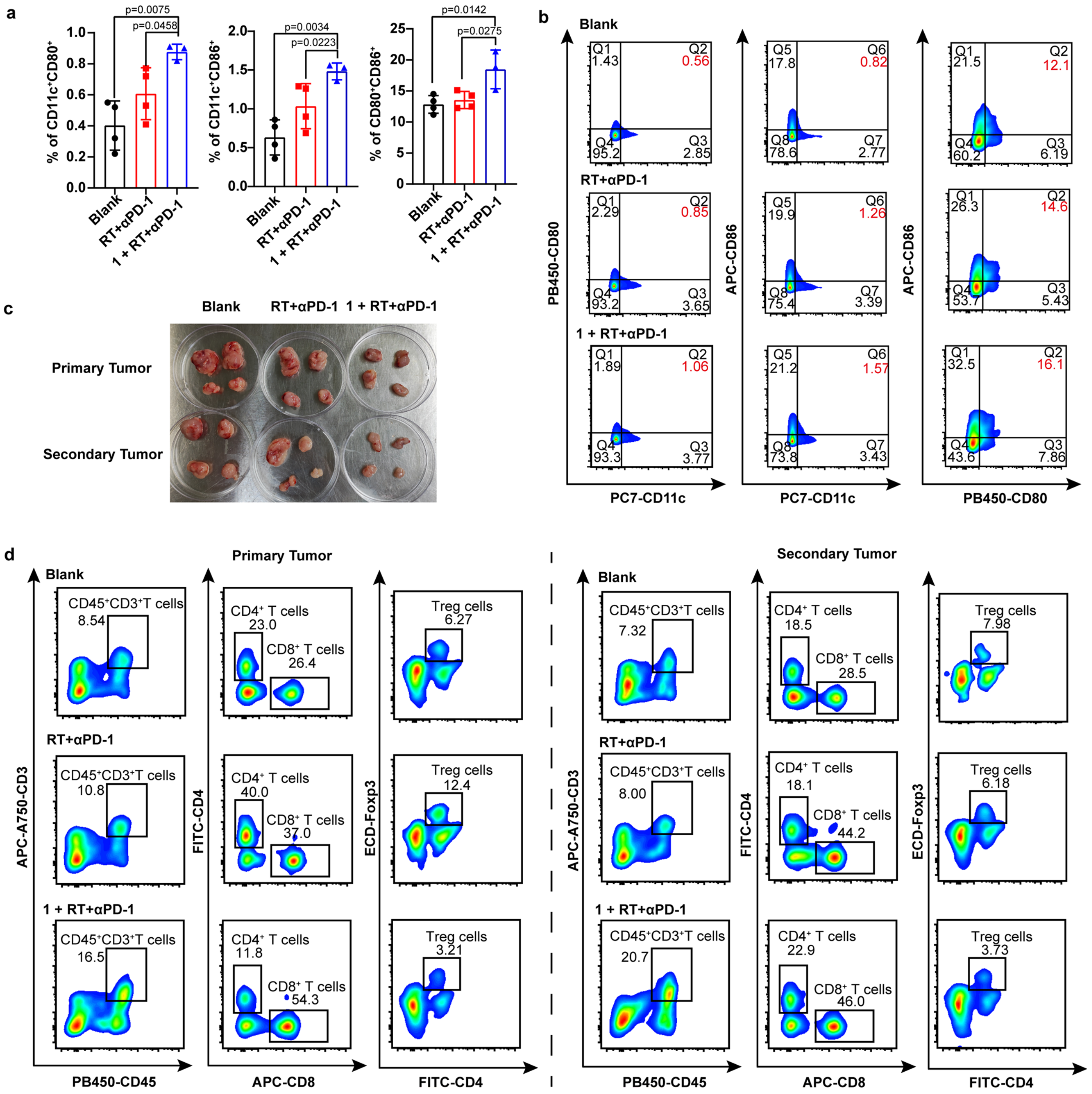

Extended Data Fig. 5 | Flow analysis of 1 sensitized RT enhancing immunotherapy and abscopal effect. **a**, Quantification of DCs maturation in TDLNs by flow cytometry indicated 1 sensitized RT enhancing abscopal effect (Blank and RT + αPD-1, n = 4; 1 + RT + αPD-1, n = 3). **b**, Corresponding representative flow plots showed DCs in TDLNs. **c**, Image of representative primary and secondary tumours. **d**, Representative flow plots of primary and secondary tumour infiltrating CD45+CD3+, CD8+and Treg (CD4+Foxp3+) cells. One-way ANOVA multiple comparisons (Tukey's multiple comparisons test) were used when more than two groups were compared. All the values in the present study are presented as the mean ± s.d., and all replicates are biological independent samples.

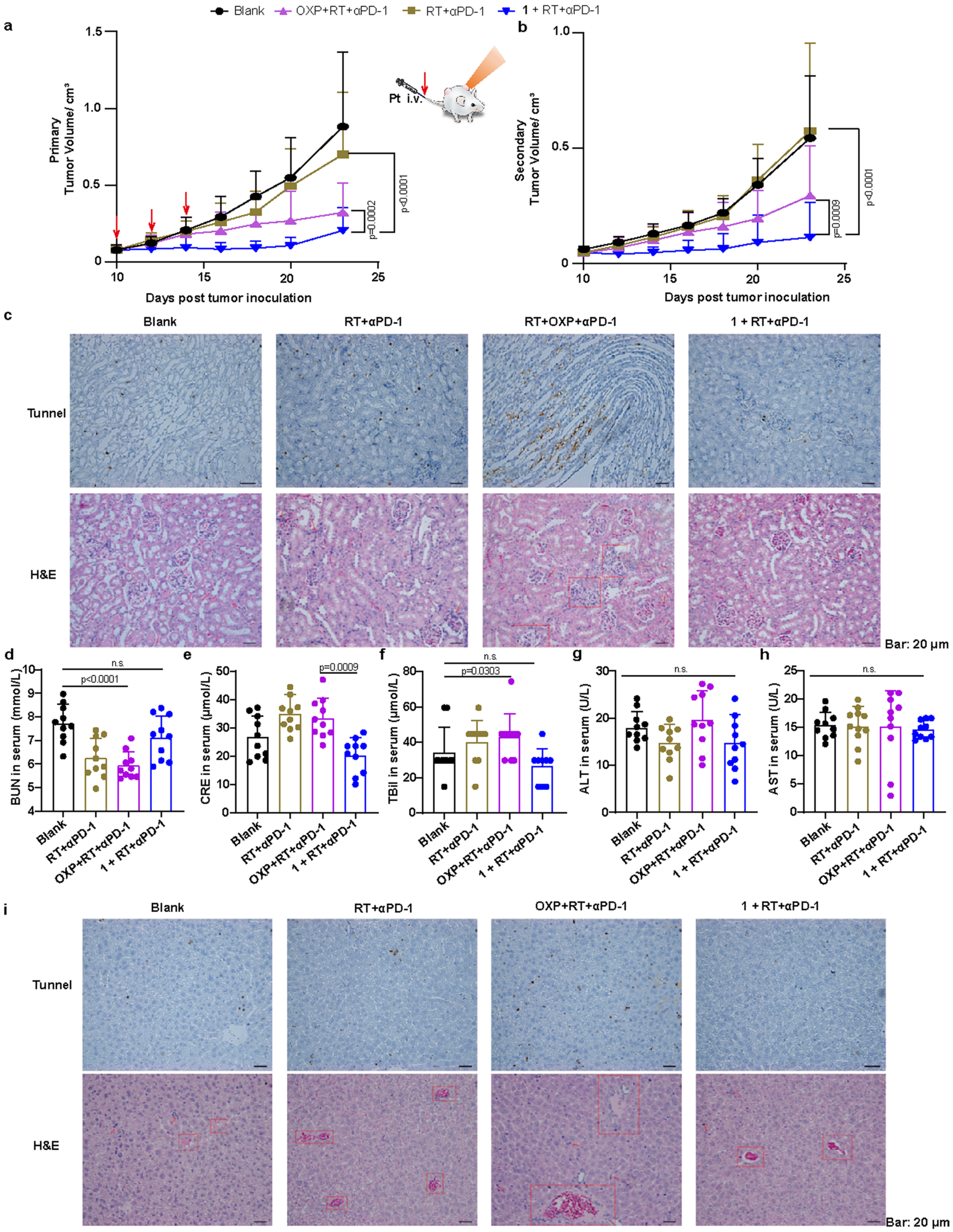

Extended Data Fig. 6 | See next page for caption.

Extended Data Fig. 6 | Platinonitrene-based radiosensitizer enhances abscopal effect that is superior to that of oxaliplatin and has reliable security. a-b, Average primary and secondary tumour growth curves showed 1 in combination with low dose of RT and αPD-1 suppress growth of bilateral tumours (n = 10). Tumour growth with the passage of time was compared by two-way ANOVA (Tukey's test). **c**, Representative TUNEL (TdT-mediated dUTP nick end labelling) and H&E (Haematoxylin and Eosin staining) section of kidneys showed 1 in combination with low dose of RT and αPD-1 would not cause the damage of kidney. **d-h**, Analysis of BUN, CRE, TBil (total bilirubin), ALT (alanine transaminase) and AST (aspartate aminotransferase) in serum showed 1 held a better biosecurity than oxaliplatin in combination with immunotherapy (n = 10). **i**, Representative TUNEL and H&E section of livers showed 1 in combination with low dose of RT and αPD-1 would not cause the damage of livers. One-way ANOVA was used for multiple comparisons (Tukey's multiple comparisons test) when more than two groups were compared. All the values in the present study are presented as the mean ± s.d., and all replicates are biological independent samples.

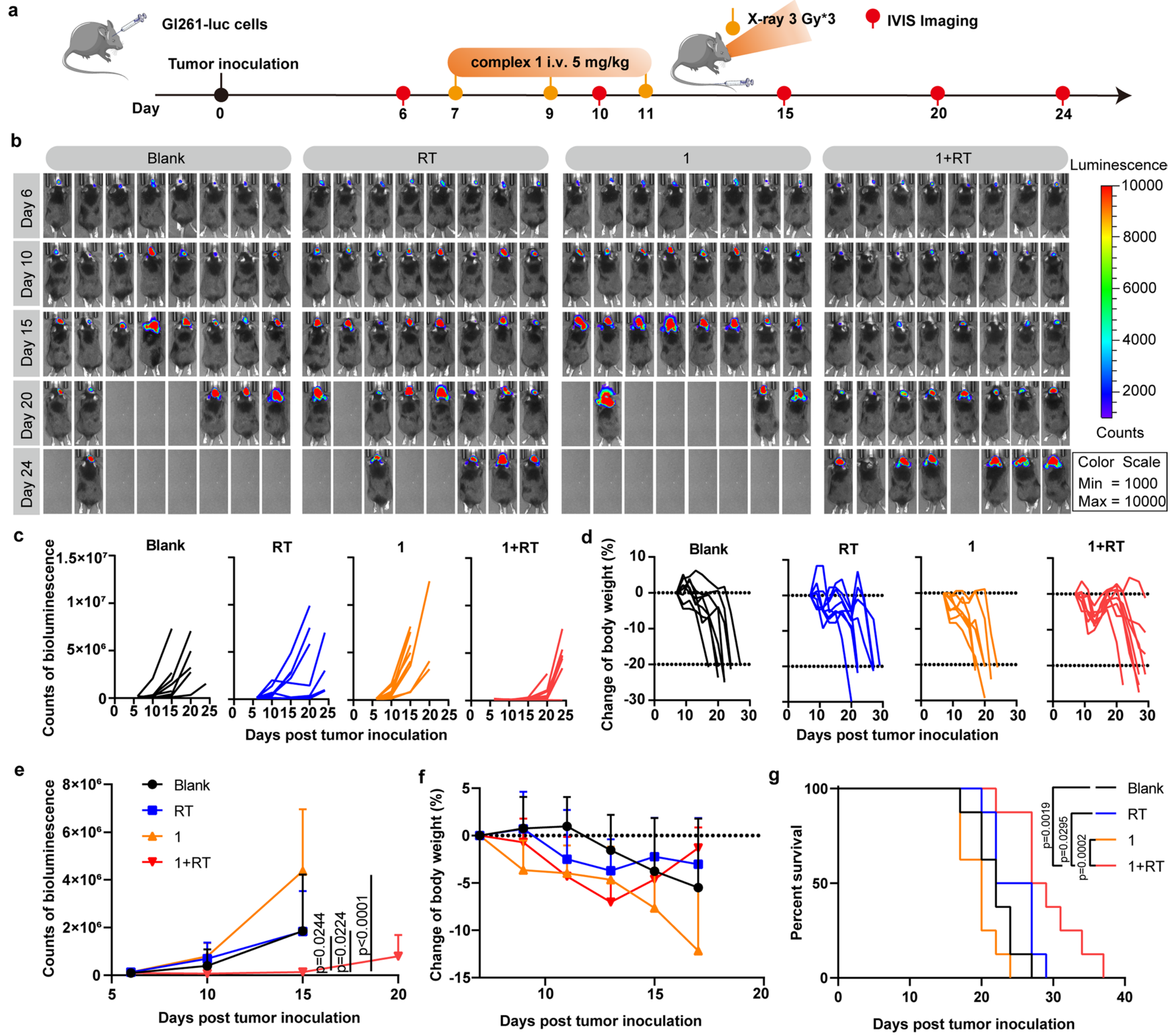

Extended Data Fig. 7 | Complex 1 sensitized RT effectively inhibits the growth of orthotopic glioblastoma. **a**, Schemes of orthotopic glioblastoma inoculation and therapies. **b**, Bioluminescence imaging suggested complex **1** sensitized RT effectively inhibited the growth of orthotopic glioblastoma (n = 8). **c**, Changes of bioluminescence counts of brain tumour area of each mouse (n = 8). **d**, Body weight change curve of each mouse (n = 8). **e**, Average bioluminescence counts change curves showed **1** sensitized RT effectively inhibited the growth of orthotopic glioblastoma (n = 8). **f**, Average body weight change curve suggested mice in 1 + RT group had the slowest weight loss (n = 8). **g**, Survival curves showed **1** sensitized RT significantly prolonged survival time of mice in orthotopic glioblastoma model (n = 8). Average bioluminescence counts change with the passage of time was compared by two-way ANOVA (Tukey's test). Differences in survival were determined for each group by the Kaplan–Meier method, and the overall P value was calculated by the log-rank test. **f**, Body weight change curve of mice (n = 8). All the values in the present study are presented as the mean ± s.d., and all replicates are biological independent samples.

Extended Data Table 1 | Parameters of bonded interactions for Platinum coordinated species of 1. Details of the atom labels can be found in Extended Data Fig. 1

Bond				
Label	**Bond**	d	k	**RE**
d_1	Pt1-N2	2.03×10^{-1}	1.7467×10^{5}	2.96
d_2	Pt1-N5	2.03×10^{-1}	1.7467×10^{5}	2.46
d_3	Pt1-N24	2.054×10^{-1}	1.3948×10^{5}	2.14
d_4	Pt1-N27	2.054×10^{-1}	1.3948×10^{5}	1.17
Angle				
Label	**Angle**	θ	k	**RE**
a_1	Pt1-N2-N3	1.2169×10^{2}	1.8906×10^{2}	0.57
a_2	Pt1-N5-N6	1.2169×10^{2}	1.8906×10^{2}	1.34
a_3	Pt1-N24-C9	1.0920×10^{2}	5.6143×10^{2}	1.10
a_4	Pt1-N24-H25	1.1119×10^{2}	2.5953×10^{2}	0.73
a_5	Pt1-N24-H26	1.1119×10^{2}	2.5953×10^{2}	1.97
a_6	Pt1-N27-C10	1.0920×10^{2}	5.6143×10^{2}	1.10
a_7	Pt1-N27-H28	1.1119×10^{2}	2.5953×10^{2}	1.63
a_8	Pt1-N27-H29	1.1119×10^{2}	2.5953×10^{2}	1.07
a_9	N2-Pt1-N5	8.6584×10^{1}	1.8694×10^{3}	0.67
a_{10}	N2-Pt1-N24	1.7827×10^{2}	1.6202×10^{3}	0.15
a_{11}	N2-Pt1-N27	9.5102×10^{1}	1.8534×10^{3}	0.11
a_{12}	N5-Pt1-N24	9.5102×10^{1}	1.8534×10^{3}	0.11
a_{13}	N5-Pt1-N27	1.7827×10^{2}	1.6202×10^{3}	0.15

To directly compare the quantum calculated structure with the classical MD results, Relative error (RE) was obtained using the following formula: $\mathrm{RE}(\%) = \left| \frac{averagedMDvalue - quantumvalue}{equantumvalue} \right| \times 100$. The relatively low RE values demonstrated that the classical forced field can reliably reproduce the structural parameters obtained based on DFT calculations at a high level.

nature portfolio

Corresponding author(s): Yuanzeng Min
Last updated by author(s): Dec 16, 2025

Reporting Summary

Nature Portfolio wishes to improve the reproducibility of the work that we publish. This form provides structure for consistency and transparency in reporting. For further information on Nature Portfolio policies, see our Editorial Policies and the Editorial Policy Checklist.

Statistics

For all statistical analyses, confirm that the following items are present in the figure legend, table legend, main text, or Methods section.

n/a	Confirmed	
☐	☒	The exact sample size (*n*) for each experimental group/condition, given as a discrete number and unit of measurement
☐	☒	A statement on whether measurements were taken from distinct samples or whether the same sample was measured repeatedly
☐	☒	The statistical test(s) used AND whether they are one- or two-sided *Only common tests should be described solely by name; describe more complex techniques in the Methods section.*
☐	☒	A description of all covariates tested
☐	☒	A description of any assumptions or corrections, such as tests of normality and adjustment for multiple comparisons
☐	☒	A full description of the statistical parameters including central tendency (e.g. means) or other basic estimates (e.g. regression coefficient) AND variation (e.g. standard deviation) or associated estimates of uncertainty (e.g. confidence intervals)
☐	☒	For null hypothesis testing, the test statistic (e.g. *F*, *t*, *r*) with confidence intervals, effect sizes, degrees of freedom and *P* value noted *Give P values as exact values whenever suitable.*
☒	☐	For Bayesian analysis, information on the choice of priors and Markov chain Monte Carlo settings
☒	☐	For hierarchical and complex designs, identification of the appropriate level for tests and full reporting of outcomes
☒	☐	Estimates of effect sizes (e.g. Cohen's *d*, Pearson's *r*), indicating how they were calculated

Our web collection on statistics for biologists contains articles on many of the points above.

Software and code

Policy information about availability of computer code

Data collection	Details are in methods part, e.g. flow cytometer CytoFLEX (Beckman), SpectraMax iD3 (Molecular Device) etc
Data analysis	Details are in methods part, e.g. GraphPad Prism Version 8, CytExpert2.3, FlowJo10.6 and etc.

For manuscripts utilizing custom algorithms or software that are central to the research but not yet described in published literature, software must be made available to editors and reviewers. We strongly encourage code deposition in a community repository (e.g. GitHub). See the Nature Portfolio guidelines for submitting code & software for further information.

Data

Policy information about availability of data

All manuscripts must include a data availability statement. This statement should provide the following information, where applicable:

- Accession codes, unique identifiers, or web links for publicly available datasets
- A description of any restrictions on data availability
- For clinical datasets or third party data, please ensure that the statement adheres to our policy

The authors declare that all data to support the results of this study are available within the the main text, extended data, and supplementary information.

Research involving human participants, their data, or biological material

Policy information about studies with human participants or human data. See also policy information about sex, gender (identity/presentation), and sexual orientation and race, ethnicity and racism.

Reporting on sex and gender	Doesn't applicable in this study as there's no human related research.
Reporting on race, ethnicity, or other socially relevant groupings	Doesn't applicable in this study as there's no human related research.
Population characteristics	Doesn't applicable in this study as there's no human related research.
Recruitment	Doesn't applicable in this study as there's no human related research.
Ethics oversight	Doesn't applicable in this study as there's no human related research.

Note that full information on the approval of the study protocol must also be provided in the manuscript.

Field-specific reporting

Please select the one below that is the best fit for your research. If you are not sure, read the appropriate sections before making your selection.

☒ Life sciences ☐ Behavioural & social sciences ☐ Ecological, evolutionary & environmental sciences

For a reference copy of the document with all sections, see nature.com/documents/nr-reporting-summary-flat.pdf

Life sciences study design

All studies must disclose on these points even when the disclosure is negative.

Sample size	No sample size calculation was performed to predetermine sample size. Sample size was chosen generally based on standard practice in the field and our long-standing experience in all types of our experimental approaches. It was specified in statistical analysis in method part.
Data exclusions	No data was exclude from all experiments.
Replication	Experiments were performed in at least three independent biological replicates under identical conditions unless stated otherwise and all attempts at replications were successful.
Randomization	All mice were allocated randomized. Sample randomization was not relevant to other parts of this study, e.g. in vitro study, as it is not necessary to randomize samples for in vitro studies.
Blinding	Single blinding was performed for all in vivo assays and data analysis, including immunohistochemistry. RNA-Seq data was analyzed single blinded. All in vitro studies were not blinded, as our experiments were not based on subjective measurements.

Reporting for specific materials, systems and methods

We require information from authors about some types of materials, experimental systems and methods used in many studies. Here, indicate whether each material, system or method listed is relevant to your study. If you are not sure if a list item applies to your research, read the appropriate section before selecting a response.

Materials & experimental systems

n/a	Involved in the study	
☐	☒	Antibodies
☐	☒	Eukaryotic cell lines
☒	☐	Palaeontology and archaeology
☐	☒	Animals and other organisms
☒	☐	Clinical data
☒	☐	Dual use research of concern
☒	☐	Plants

Methods

n/a	Involved in the study	
☒	☐	ChIP-seq
☐	☒	Flow cytometry
☒	☐	MRI-based neuroimaging

Antibodies

Antibodies used	All antibodies used and their dilution in the manuscript are listed in the Methods part .
Validation	All antibodies for flow cytometric analysis were well-commercialized clones and already validated by manufacturers. They are routinely used in our lab. We don't validated by ourselves.

Eukaryotic cell lines

Policy information about cell lines and Sex and Gender in Research

Cell line source(s)	CT26 cell lines and 4T1 cell lines were purchased from Cell Bank of Chinese Academy of Sciences (Shanghai, China). Gl261-luc cell line was purchased from Yuanjing Biotechnology Co., Ltd (Guangzhou, China).
Authentication	Cell lines were used as received and not authenticated.
Mycoplasma contamination	All cell lines is usually tested for mycoplasma upon being received and cells in this study are negative for mycoplasma.
Commonly misidentified lines (See ICLAC register)	No cell line used in the manuscript is listed in ICLAC database

Animals and other research organisms

Policy information about studies involving animals; ARRIVE guidelines recommended for reporting animal research, and Sex and Gender in Research

Laboratory animals	Female BALB/c mice (6-8 weeks old, 20 gram) and C57BL/6J mice (female, 6-8 weeks) were purchased from Shanghai Slac Laboratory Animal Co., Ltd. (Shanghai, China). C57BL/6-Foxp3tm1Flv/J mice were obtained from the gift of Prof. Shu Zhu from the University of Science and Technology of China. They were raised in specific-pathogen-free animal rooms with light and dark shifts every 12 hours, and were provided with adequate food and water sources.
Wild animals	This study did not include any wild animals.
Reporting on sex	This study did not include any reporting on sex.
Field-collected samples	This study did not involve any field-collected samples.
Ethics oversight	Animal research was conducted in compliance with the procedures approved by the China Experimental Animal Care Commission at the University of Science and Technology of China and complied with all relevant ethical regulations.

Note that full information on the approval of the study protocol must also be provided in the manuscript.

Plants

Seed stocks	Doesn't applicable in this study as there's no related research.
Novel plant genotypes	Doesn't applicable in this study as there's no related research.
Authentication	Doesn't applicable in this study as there's no related research.

Flow Cytometry

Plots

Confirm that:

☒ The axis labels state the marker and fluorochrome used (e.g. CD4-FITC).

☒ The axis scales are clearly visible. Include numbers along axes only for bottom left plot of group (a 'group' is an analysis of identical markers).

☒ All plots are contour plots with outliers or pseudocolor plots.

☒ A numerical value for number of cells or percentage (with statistics) is provided.

Methodology

Sample preparation	Doesn't applicable in this study as there's no related research.
Instrument	Doesn't applicable in this study as there's no related research.
Software	Doesn't applicable in this study as there's no related research.
Cell population abundance	Doesn't applicable in this study as there's no related research.
Gating strategy	Doesn't applicable in this study as there's no related research.

☒ Tick this box to confirm that a figure exemplifying the gating strategy is provided in the Supplementary Information.